

Elevated and cryogenic temperature micropillar compression of magnesium-niobium multilayer films

K. Thomas ^{a,b}, G. Mohanty ^c, J. Wehrs ^a, A. A. Taylor ^d, S. Pathak ^e, D. Casari ^a, J. Schwiedrzik ^a, N. Mara ^f, R. Spolenak ^b, J. Michler ^a

^a *Empa, Swiss Federal Laboratories for Materials Science and Technology, Laboratory for Mechanics of Materials and Nanostructures, Feuerwerkerstrasse 39, CH-3602 Thun, Switzerland*

^b *Laboratory for Nanometallurgy, Department of Materials, ETH Zurich, Vladimir-Prelog-Weg 5, CH-8093 Zurich, Switzerland*

^c *Materials Science and Environmental Engineering, Tampere University, 33014 Tampere, Finland*

^d *University of California, Santa Barbara, Materials Department, Engineering II Building, 1355, Santa Barbara, CA 93106-5050, USA*

^e *Chemical and Materials Engineering, University of Nevada, Chemical and Materials Engineering, 1664 N. Virginia Street, Reno, NV 89557, USA*

^f *University of Minnesota, Department of Chemical Engineering and Materials Science, 421 Washington Ave. SE, Minneapolis, MN 55455-0132, USA*

E-mail addresses for correspondence:

gaurav.mohanty@tuni.fi;
johann.michler@empa.ch

1. Introduction

Periodic bilayers are a specific class of multilayer films in which two materials are alternately deposited onto a substrate, keeping the individual layer thickness of each material constant. Periodic bilayer thin films are generally useful as test structures for investigating the role of interfaces and size effects in addition to their use as optical elements (Bragg reflectors [1], Göbel X-Ray mirrors [2], and waveguides [3]) and in semiconductor devices (lasers [4] and LEDs [5]). They are frequently used to investigate the mechanical strengthening observed at nanoscale periodicities, where a total film thickness on the micron scale enables nanoindentation, micropillar compression, micro-tensile testing, or a number of other mechanical tests to be performed. Loads applied perpendicular to the bilayer stack then effectively test a series of bilayers, allowing the mechanical properties of a single bilayer to be extracted through comparison with strengthening models.

Factors determining the strength of multilayers include the inherent strength of the constituent materials, differences between the elastic moduli of the materials used, the thickness of each layer, and the type of interface (coherent, incoherent, etc.). In metallic multilayers the various strengthening mechanisms function by inhibiting dislocation movement [6]. At thickness on the order of a few hundred nanometers to microns, dislocation pile-up provides strength in a fashion similar to the classical Hall-Petch relationship. Further reduction of layer thickness to tens of nanometers provides sufficient confinement to permit only a single dislocation to fit within each layer, bowing between the upper and lower interfaces. Misfit dislocations can reside at the interfaces to relieve some of the local stress [7]. Dislocation bowing is often described as being analogous to the Orowan mechanism in particle-reinforced composites. Once layer thicknesses reach the single-digit nanometer or thinner range, the resistance of the interface to dislocation movement and the nature of the interface become dominant. Depending on the constituent materials, this can result in either a strengthening or softening effect [8]. One notable exception to this general rule is the case in which there is a large elastic mismatch between the two materials. In this case it is not dislocations which are responsible for hardening, but rather the buildup of hydrostatic stress within the material with a lower modulus of elasticity. The stiffer material experiences a lateral tensile stress while the more compliant material is subject to the resultant compressive stress [9]. These stresses are largest in the center of the pillar and decay

near the pillar edges, where the interface no longer provides as much lateral constraint. These “soft-hard” material combinations are especially interesting as they provide much higher strengths than would ordinarily be achievable with such high proportions of the softer material.

In addition to materials strengthening, interfacial energy reduction can even stabilize otherwise unstable phases in one of the constituent materials. This polymorphic transformation is referred to as pseudomorphism, and can be considered an interface-stabilized allotrope. Stable pseudomorphs are formed when the sum of the strain energy due to coherency stress, the applied stress, and the energy penalty of forming dislocation arrays is minimized. Examples of materials systems which exhibit polymorphic transformation in multilayers include Mg-Nb [10], Zr-Nb [11,12], and Ti-Al [13,14]. Since the driving force for phase transformation is a reduction of interfacial energy, either of the two components can be made to adapt to the phase of the other by selecting appropriate layer thicknesses. Bi-phase transition diagrams show which phases will be present as a function of bilayer thickness and the volume fraction of one component [15]. Calculated bi-phase transition diagrams generated using a thermodynamic model for energy show good agreement with experimental work and are available for a number of materials systems [16]. The stabilization of pseudomorphs generally requires a volumetric ratio other than 1:1 [16], therefore future studies will benefit from investigating the effects of both layer thickness and volumetric ratio.

All combinations of body-centered cubic (BCC), face-centered cubic (FCC), and hexagonal close-packed (HCP) transitions have been observed, but the HCP to cubic transitions are especially of interest. Polycrystalline HCP metals tend to be brittle due to the limited number of slip systems available, whereas cubic metals can undergo significant plastic deformation before failure. By inducing a pseudomorphic transformation within a normally HCP metal it should be possible to capitalize on the metal's desirable properties while foregoing the usual drawback of limited plasticity. Niobium is an ideal partner for this stabilization due to its mutual insolubility with magnesium and its BCC crystal structure, though an alternative material would be needed for applications seeking to capitalize on magnesium's low density for lightweight applications since niobium is nearly five times denser than magnesium. This work seeks to investigate the operative deformation mechanisms present in the BCC magnesium phase to determine the

potential impact this phase stabilization has on the strength and ductility of a multilayer composite.

2. Experimental

2.1. Sample Preparation

Magnesium-niobium multilayer thin films were deposited in a sputtering chamber built by H.V.A. (High Vacuum Apparatus Mfg. Inc., Hayward, California, USA). Substrates were mounted to a vertical-axis rotating spindle which can be rotated to face one of four target cusps. Large (6-inch diameter) targets were positioned at a four-inch working distance from the substrates in a lateral sputtering configuration (neither sputter-up or sputter-down). The small working distance and large target size enable homogeneous film thicknesses to be deposited without rotating the substrates during depositions. Square silicon chips with roughly 1 cm side length were cleaved from a 4-inch (100) wafer to be used as substrates. These substrates were rinsed with acetone and deionized water before being blow-dried with compressed air to remove particles generated in the cleaving process. A total film thickness of 5 μm was targeted, with nominal layer thicknesses of 5 nm for one film and 50 nm for the other. The sputtering conditions are given in Table 1.

Table 2: Sputter deposition conditions

	film 1	film 2
targeted individual layer thickness	5 nm	50 nm
base pressure	5-10-7 Torr	5-10-7 Torr
deposition pressure	6 mTorr	6 mTorr
Nb deposition power	300 Watts	300 Watts
Mg deposition power	300 Watts	300 Watts
Nb cycle duration	9.30 s	93.0 s
Mg cycle duration	2.03 s	20.3 s
# of bilayer cycles	500	50
nominal film thickness	5 μm	5 μm

After film deposition, the samples were mounted on aluminum stubs using a high-temperature silver adhesive (Aremco Pyro-Duct 597TM-A). The samples were cured at 100°C for two hours to ensure good bonding without encouraging grain growth within the film. A focused ion beam (FIB) workstation (Tescan Vela) was used for milling the

micropillars using a three-step process. First, stepped circles with an outer radius of 20 μm and inner radius of 5 μm were milled using an accelerating voltage of 30 kV and a current of 6 nA, stopping when the crater floor first reached the interface between the film and the substrate. Second, an annulus was milled at 30 kV and 1.6 nA to reduce the pillar diameter and sidewall taper. Finally, a polishing circle was used under the same milling conditions as in the previous step to achieve the final pillar diameter. The diameter was selected to be 40% of the film thickness, resulting in pillars with a nominal aspect ratio of 2.5. A total of 56 micropillars were milled in each of the two samples. The same FIB workstation was used to produce the cross-sectional lamella for transmission electron microscopy (JEOL JEM-2200FS) by the lift-out process.

2.2. Microstructure analysis

The film thicknesses were determined using three independent methods: step height measurement using a stylus profilometer (Altisurf 500), examination of FIB-prepared (Tescan Vela) film cross sections by both scanning (Hitachi S-4800) and transmission electron microscopy (Jeol 2200 FS), and X-Ray Reflectometry (XRR) (Bruker D8 Discover). The sputter rates were initially determined after depositing separate elemental magnesium and niobium films, each with a thickness of roughly 100 nm. A thin strip of tape was placed across each substrate prior to deposition and peeled away after deposition. The step height was then measured using a stylus profilometer. The films are referred to by their nominal individual layer thicknesses of 5 and 50 nm for the remainder of this paper, though the layer and film thicknesses determined by XRR and as reported in the results section are considered to be the more accurate values.

A Bruker Discover D8 with Cu K_{α} radiation was used for both the XRR and XRD measurements. For the XRD scans an offset Bragg-Brentano arrangement was used to measure a 2θ range from 20° to 100° with a step size of 0.05° . A 2° offset was utilized for the ω - 2θ scans to suppress diffraction peaks from the single-crystalline silicon substrate. For the XRR measurements data was collected from 2θ values of 0.25° to 4.25° with a step size of 0.025° for the 5 nm films and 0.0076° for the 50 nm films. Thicker layers require improved resolution to adequately capture the narrower oscillations. The collection time was increased at higher angles to partially compensate for the decreased signal intensity.

2.3. Mechanical characterization

All micropillar compression experiments were performed using an *in situ* indenter (Alemnis AG, Switzerland), as previously described in detail [17]. This experimental platform allows for displacement-controlled tests to be performed across a wide range of temperatures and strain rates operating *in situ* within a Zeiss DSM 962 Scanning Electron Microscope (SEM). Strain rate sensitivity (m) and activation volume (V) were determined using Strain Rate Jump (SRJ) tests as originally performed on metallic (Cu-Ni) multilayers by Carpenter *et. al* [18] and since used regularly [19]. These SRJ tests are generally more reliable than comparing constant strain rate tests on separate micropillars due to stochastic variation in small-scale test specimens. Room temperature micropillar compression SRJ tests began at baseline strain rate of $9 \times 10^{-4} \text{ s}^{-1}$. Shortly after the onset of plastic deformation the strain rate was dropped abruptly to $5 \times 10^{-5} \text{ s}^{-1}$. Subsequent jumps to strain rates of $2 \times 10^{-4} \text{ s}^{-1}$, $5 \times 10^{-5} \text{ s}^{-1}$, and $9 \times 10^{-4} \text{ s}^{-1}$ were performed once the deformation had stabilized. Four SRJs were performed on each micropillar, enabling three strain-rate sensitivity values to be calculated.

Elevated temperature tests were performed at five different temperatures: 20, 72.5, 150, 200, and 250 °C. For magnesium, with a melting temperature of 650°C, these temperatures correspond to homologous temperatures of 0.32, 0.38, 0.46, 0.51, and 0.57. Five micropillars were compressed at each temperature to ensure sufficient statistical data could be collected. Prior to heating the first five pillars were compressed at 20 °C to establish if any microstructural changes occur within the samples during the elevated temperature tests. Both the sample and indenter were then heated to the maximum temperature of 250 °C and allowed to reach thermal equilibrium over the course of approximately one hour before compressing the next set of five micropillars. The temperature was then stepped down incrementally following the same procedure, concluding with an additional five micropillars compressed at 20 °C. Performing the highest temperature tests first helps to minimize the potential microstructural changes which may occur between tests. No visible signs of sample oxidation were observed during the elevated temperature testing.

Cryogenic micropillar compression tests were also performed at -70°C and -30°C. The same *in situ* indenter used for the elevated temperature tests was modified to permit cryogenic tests to be performed as well [20]. Both the sample and the flat-punch

indenter are cooled by pumping vapor from a 25-liter cryogenic storage dewar filled with liquid nitrogen. Resistive heaters and thermocouples for temperature feedback are then used to ensure that the sample and indenter tip are in thermal equilibrium before the compression experiments are performed. A separate sample (deposited during the same sputtering run) was attached to an aluminum stub using Stycast 2850FT adhesive. The entire sample was then sputtered with a thin (<5nm) layer of gold to ensure that sufficient SEM image quality could be obtained to reliably align the sample.

All micropillars were imaged using a Hitachi S-4800 SEM both prior to compression (to determine the exact pillar dimensions) and after compression (to observe the deformation mode). As there is a slight pillar taper from annular milling, the stress was calculated using the upper diameter of each micropillar. Strain was determined using the total displacement relative to the film thickness. The yield stress was taken at 1% strain rather than the conventional 0.2% in order to capture yielding at the top of the pillar and not at the collapse of the bottom layer.

3. Results

3.1. X-ray diffraction

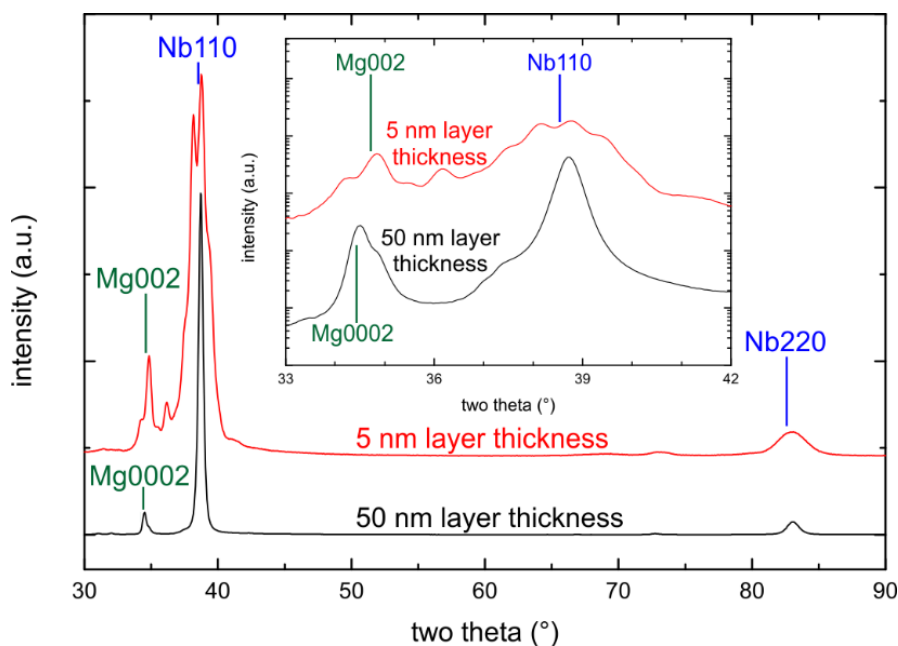


Figure 1: Bragg-Brentano XRD patterns for both 5 and 50 nm layer thicknesses in Mg-Nb multilayers. Superlattice peaks are apparent between 33° and 42° for the films with a layer

thickness of 5 nm, indicating an epitaxial relationship between Mg and Nb for thin layer thicknesses.

The XRD patterns for the magnesium-niobium multilayers, shown in Figure 10, exhibit a number of interesting features. For both samples the Nb {110}, Nb {220}, and basal Mg peak ({002} for the 50 nm films and {0002} for the 5 nm films) are much more pronounced than any other peaks. This indicates a strong {110} texture in the Nb layers, as is often observed for a BCC material prepared via physical vapor deposition (PVD). The 50 nm Mg layers exhibit a {002} texture, with the c-axis perpendicular to and the close-packed planes parallel to the substrate. The 5 nm Mg layers exhibit a {0002} texture since the magnesium adopts a BCC crystal structure. Identification of which magnesium pseudomorph is present in the sample is difficult using only the Bragg-Brentano XRD scans since higher-order superlattice peaks are visible between 33° and 42°. These peaks are a product of X-rays diffracted from the superlattice, where the layer thickness effectively acts as a large unit cell [21]. Superlattice peaks are commonly observed in periodic bilayer structures with individual layer thicknesses between 1 and 15 nm [22]. Thicker layers will result in only classical XRD peaks while thinner layers tend to produce individual, broad peaks. At sub-nanometer layer thicknesses adjacent peaks can meld together to form a single, broad peak. The spacing, position, and intensity of these superlattice peaks can be used to precisely determine the layer thickness and interface roughness in superlattice structures [23]. A complex fitting operation, as described in Schuller's *New Class of Layered Materials* [21], can be conducted to obtain precise information regarding the structure of the multilayer film. For cases where only a simple estimate of the individual layer thickness is required, this can be obtained using

Equation 5:

$$\sin \theta_{\pm} = \sin \theta_B \pm \frac{n\lambda}{2\Lambda} \quad \text{Equation 1}$$

where θ_{\pm} is the position of the satellite peak, θ_B is the position of the main Bragg diffraction peak, n is the order of the satellite peak, λ is the X-ray wavelength, and Λ is the bilayer thickness.

Equation 5 was originally developed to utilize only the position of the first satellite peak [24], though it was later extended to include additional satellite peaks [25]. It is not uncommon for there to be some minor

discrepancy between the values calculated from the satellite peaks, though in general the difference is quite small. After algebraic rearrangement of this equation the bilayer thickness for the nominally 5 nm thick layer film was calculated as 8.8 nm. This value is an average from the seven satellite peaks, which varied from 8.3 to 9.4 nm.

3.2. X-ray reflectometry

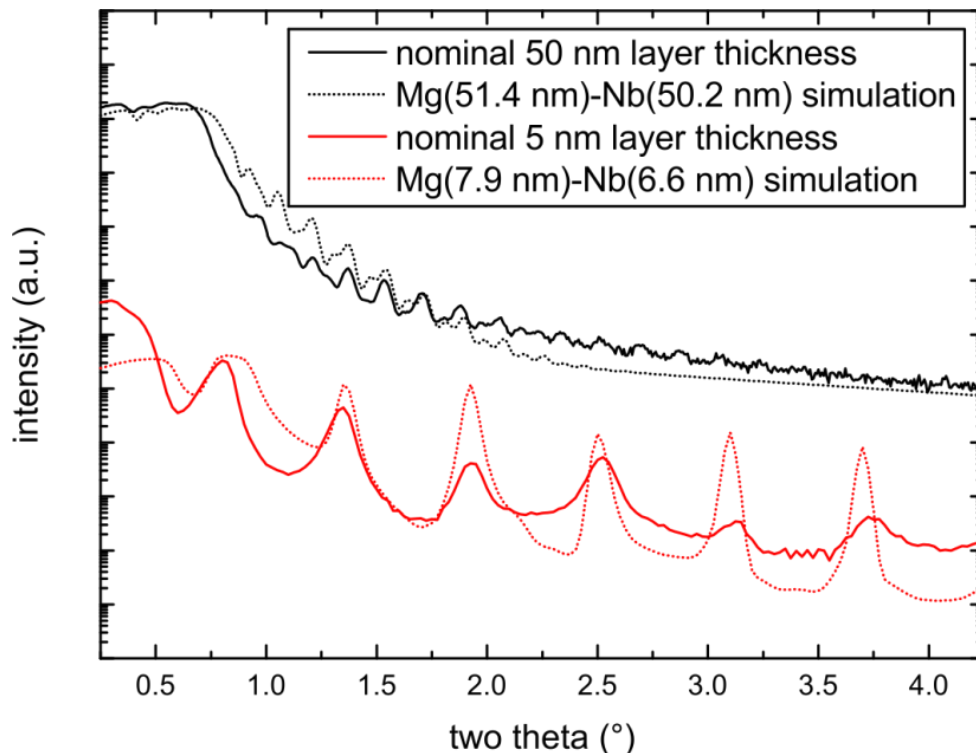


Figure 2: X-Ray Reflectometry (XRR) curves, both as measured and as simulated for Mg-Nb multilayers with nominal 5 and 50 nm layer thicknesses.

The XRR curves for both samples are shown in Figure 11. The thickness of the layers can be determined simply using the Fast Fourier Transform (FFT) of each curve, or more precisely by fitting a model to the data. Using the FFT approach, frequencies of 49.9 and 94.3 nm were determined for the nominally 50 nm thick layers while frequencies of 6.1, 14.7, 20.5, and 28.7 nm were strongly detected for the nominally 5 nm thick layers. Since the FFT can contain secondary reflections it is necessary to use the simulation approach to precisely determine the layer thickness. The results of the XRR simulations are shown alongside the measured data in Figure 11.

Bruker Leptos software was used to construct a simple 2D model for the simulation, consisting of alternating magnesium and niobium layers atop a silicon substrate. The layer thickness and interface roughness were the only adjustable parameters and a

genetic algorithm was used to perform the necessary fitting. The film with nominally 5 nm thick layers was shown to consist of 7.9 nm thick magnesium layers and 6.6 nm thick niobium layers with an interface roughness of roughly 0.3 nm. The film with nominally 50 nm thick layers was shown to consist of 51.4 nm thick magnesium layers and 50.2 nm thick niobium layers with an interface roughness of 2.0 nm. These values are an average over the sample and are expected to vary somewhat locally. The layer thicknesses determined by XRR are representative of the entire sample while the TEM analysis gives an indication of the thickness variability across the sample. In both films the critical angle for total external reflection was somewhat lower than that calculated by simulation. This is likely due to the formation of a partial MgO layer atop the film. Fitting was also performed using a model which included a thin MgO layer, but in general the fit was inferior to the simpler model. Realistically the interface roughness would increase with distance from the silicon substrate, but for the sake of simplicity was considered to be constant among all of the layers.

3.3. Cross-sectional TEM

A horizontal cross-section TEM shows a clearly defined multilayer structure as seen in

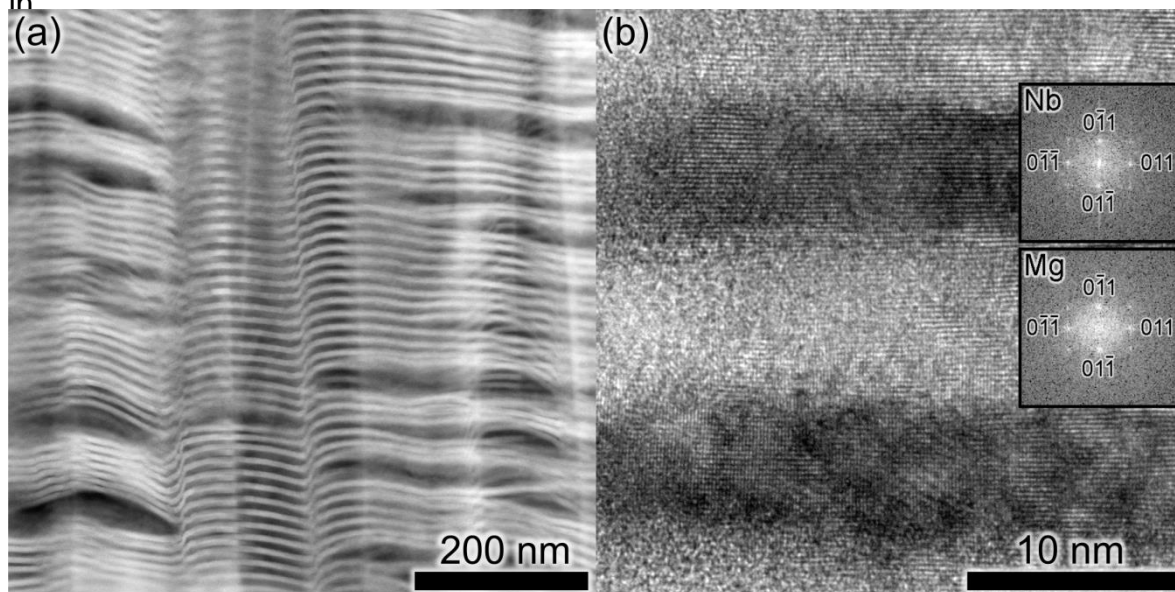


Figure 12(a).

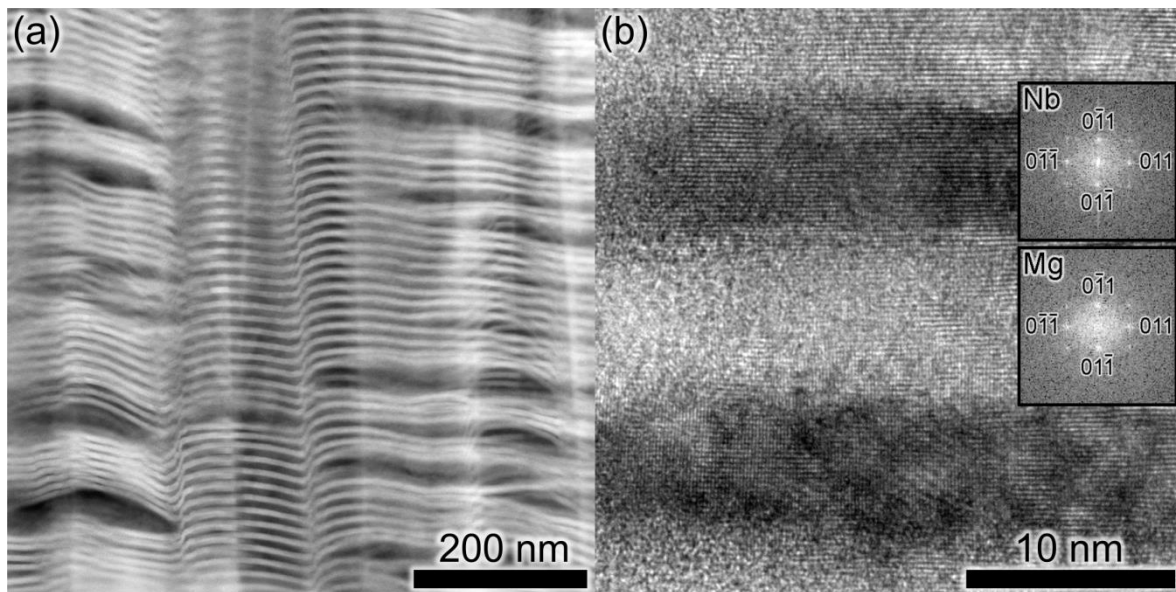


Figure 3: Cropped and rotated (a) HAADF-STEM and (b) HRTEM image with FFT inset of Mg-Nb multilayer with 5 nm layer thickness

Based on this micrograph, the average magnesium layer thickness is 7.4 nm while the average niobium layer thickness is 7.2 nm. The average bilayer thickness of 14.6 nm is in good agreement with the 14.5 nm bilayer thickness determined by XRR. The appearance of waviness is a product of the curtaining effect produced when milling the TEM lamella with the FIB [26]. Surface micrographs for the 5 nm layer thickness films show a characteristic brain-like wrinkle pattern, seen in Figure 13. The presence of these wrinkles makes it challenging to avoid the curtaining effect and indicate that some columnar porosity may be present within the sample. This microstructure was not observed in any of the cross-sectional views of the film, so it is considered to be a growth phenomenon present only at the film surface.

The epitaxial relationship between the magnesium and the niobium layers can be observed in

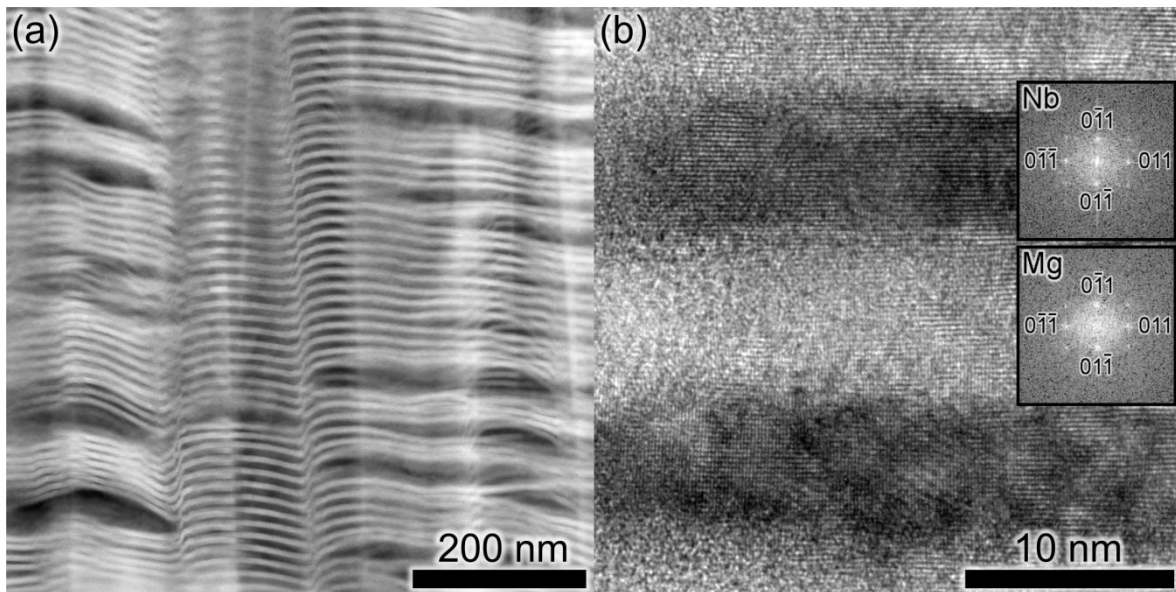


Figure 12(b). The magnesium layers (light) exhibit a BCC crystal structure to realize a classic cube-on-cube epitaxy, as seen in the inset Fast Fourier Transform (FFT) images.

3.4. Mechanical Testing – Micropillar Compression

3.4.1. Strain Rate Jump

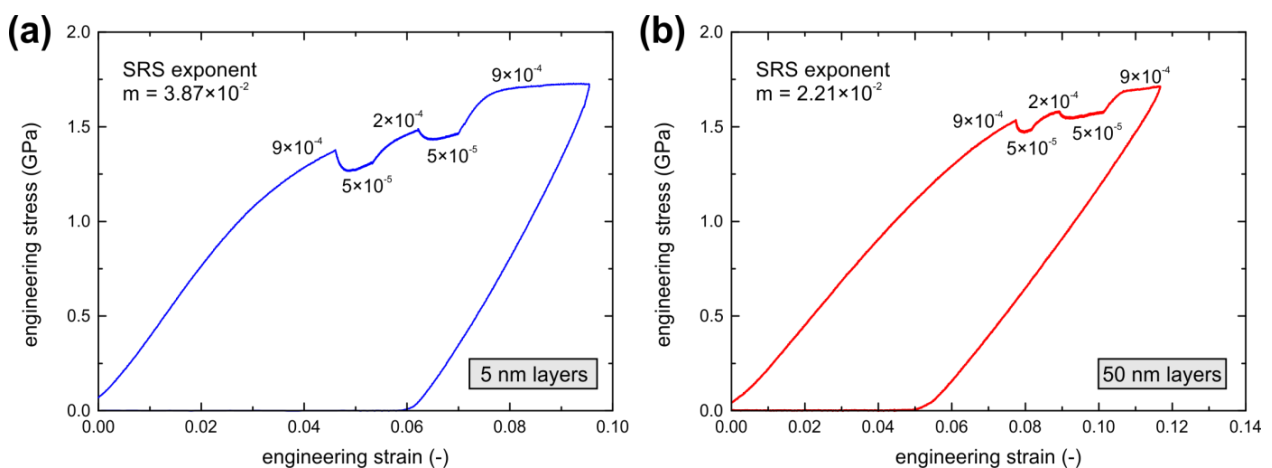


Figure 4: Strain Rate Jump (SRJ) results for Mg-Nb multilayers with (a) 5 nm layer thickness and (b) 50 nm layer thickness

Typical stress-strain curves for the SRJ tests are shown in Figure 14. The strain reached before the ultimate yield strength is reached tends to be short, necessitating

that all SRJs be performed before 10-15% engineering strain was reached. There is a small tail at the beginning of the loading curve which corresponds to the upper surface of the pillar conforming to the diamond flat punch as the indenter comes into contact with the micropillar. No erosion of the indenter or chemical reaction between the sample and diamond indenter was observed. Typical stress-strain behavior was observed on a preliminary micropillar compression test to establish the strain necessary for plastic deformation to begin and determine how long each strain-rate should be applied between the strain-rate jumps. In general the transients were not as sharp as those observed in other material systems [19,27], so at most four SRJs could be performed for a given micropillar. Strain rate sensitivity is observed for both 5 and 50 nm thick layers, though it is more pronounced in the 5 nm layers.

$$m = \left. \frac{\partial \ln \sigma}{\partial \ln \dot{\epsilon}} \right|_T \quad \text{Equation 2}$$

The strain rate sensitivity (SRS) exponent, m , is calculated from a uniaxial strain rate jump test by using Equation 6 [28,29]. The results of this evaluation demonstrate that the thinner layers exhibit larger sensitivity to strain rate. In addition to the SRS exponent, another useful metric for evaluating the operative deformation mechanism is the apparent activation volume. The apparent activation volume is inversely proportional to the strain rate sensitivity exponent and is given by Equation 7 [29,30].

$$V_{activation, apparent} = \frac{\sqrt{3}kT}{m\sigma_f} \quad \text{Equation 3}$$

Both the SRS and apparent activation volume will exhibit some temperature dependency, but for the sake of simplicity the results from the room temperature SRJ tests are applied to calculations at elevated temperatures as well. Activation volumes commonly interpreted as belonging to grain-boundary diffusion are typically less than 10 times the cube of the Burger's vector. Taking a Burger's vector value of 0.3192 nm for the 50 nm magnesium layers, the room temperature activation volume is 5.58 times the cube of the Burger's vector. For the 5 nm magnesium layers a lattice constant of 0.3574 nm was used as calculated by density functional theory (DFT) simulations[31,32]. The activation volume at room temperature for the 5 nm layers is 2.78 times the cube of the Burger's vector.

3.4.2. Elevated Temperature Micropillar Compression

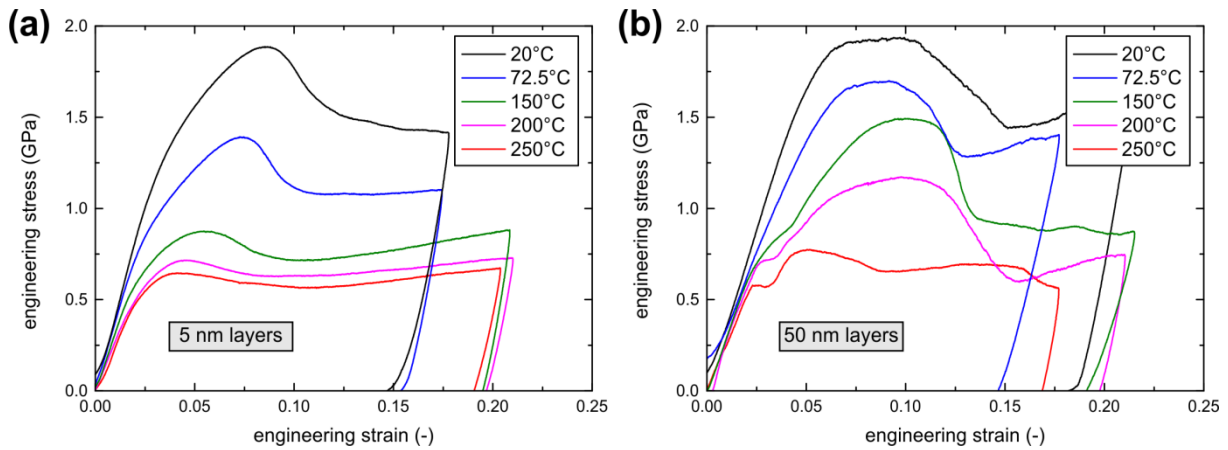


Figure 5: Engineering stress-strain curves for Mg-Nb multilayers with (a) 5 nm layer thickness and (b) 50 nm layer thickness at elevated temperatures

Typical engineering stress-strain curves from the elevated temperature tests are shown in Figure 15. For both samples the yield stress predictably decreases with increasing temperature, though there are differences in the general yield behavior. For the 5 nm layers the elastic region is initially linear after the pillar surface has flattened, but then exhibits a gradual transition from the elastic regime to the point of highest stress. At higher temperatures this effect is less pronounced and a steady engineering stress is observed up to engineering strains of 20%. The 50 nm thick layers exhibit a comparatively sharp transition from the elastic to plastic regime, followed by a moderate strain-hardening plateau before the ultimate compressive stress is reached. At temperatures at and above 150°C, a characteristic kink is observed which becomes more pronounced at higher temperatures. Reviewing the in-situ SEM videos, this kink is shown to be associated with the collapse of the lowest magnesium layer.

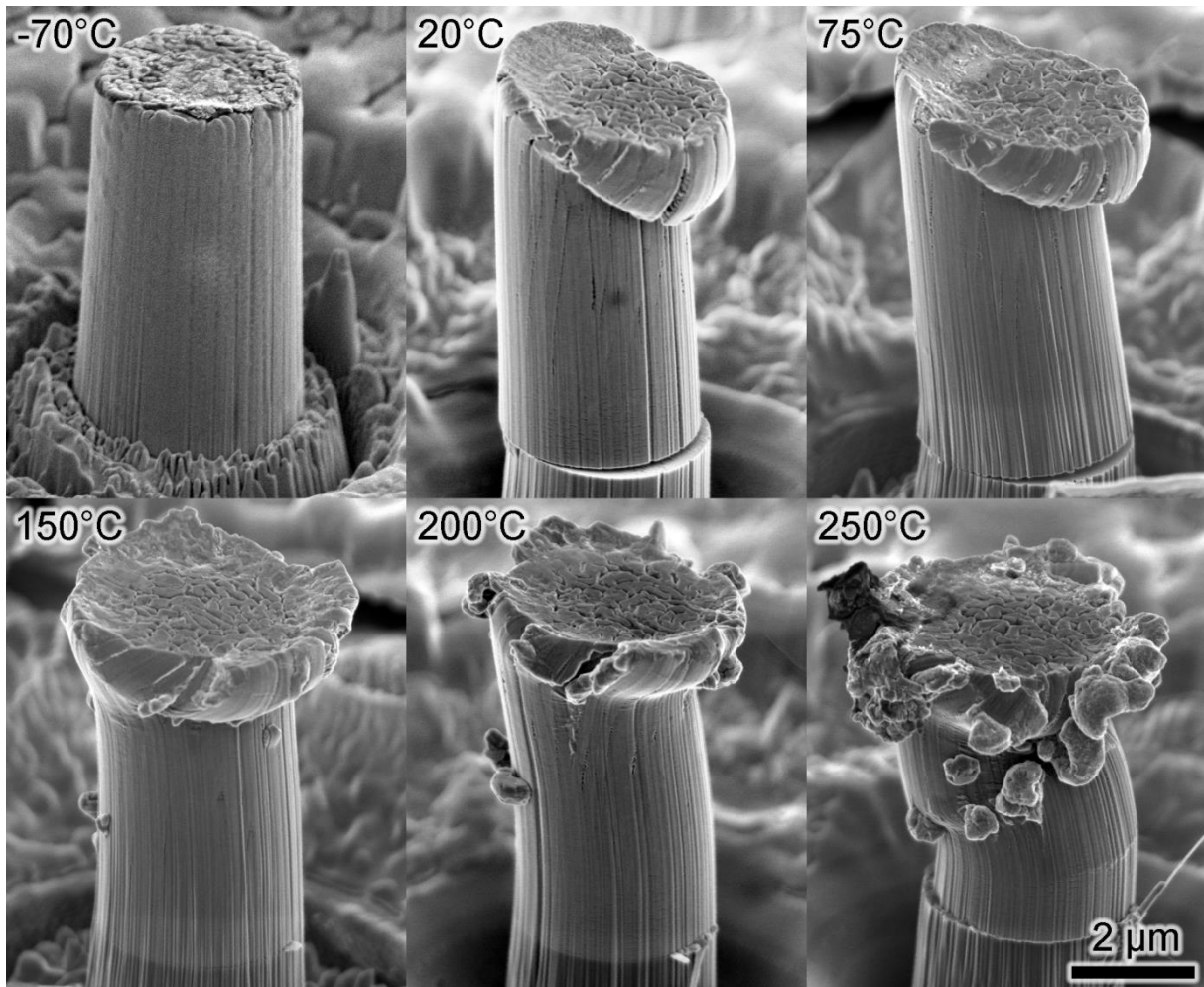


Figure 6: Micropillars with 5 nm layer thickness compressed at various temperatures

Post-mortem micrographs for characteristic micropillars compressed at elevated temperatures are given in Figure 16 and Figure 17. The 5 nm layer thickness samples deform in a similar fashion across the entire temperature range: plastic deformation is largely confined to the upper portion of the pillar, where taper from the FIB-milling process results in a smaller diameter and higher stress. At the two lower temperatures a shear band has formed near the top of the pillar which ultimately results in a large lateral force on the rest of the pillar. This has led to the separation of the pillar from its substrate pedestal, but occurs at strains above 10 percent and has no impact on the yield strength calculations. At higher temperatures and large strains, beginning at 150°C, signs of magnesium extrusion and coalescence into beads on the micropillar surface can be observed.

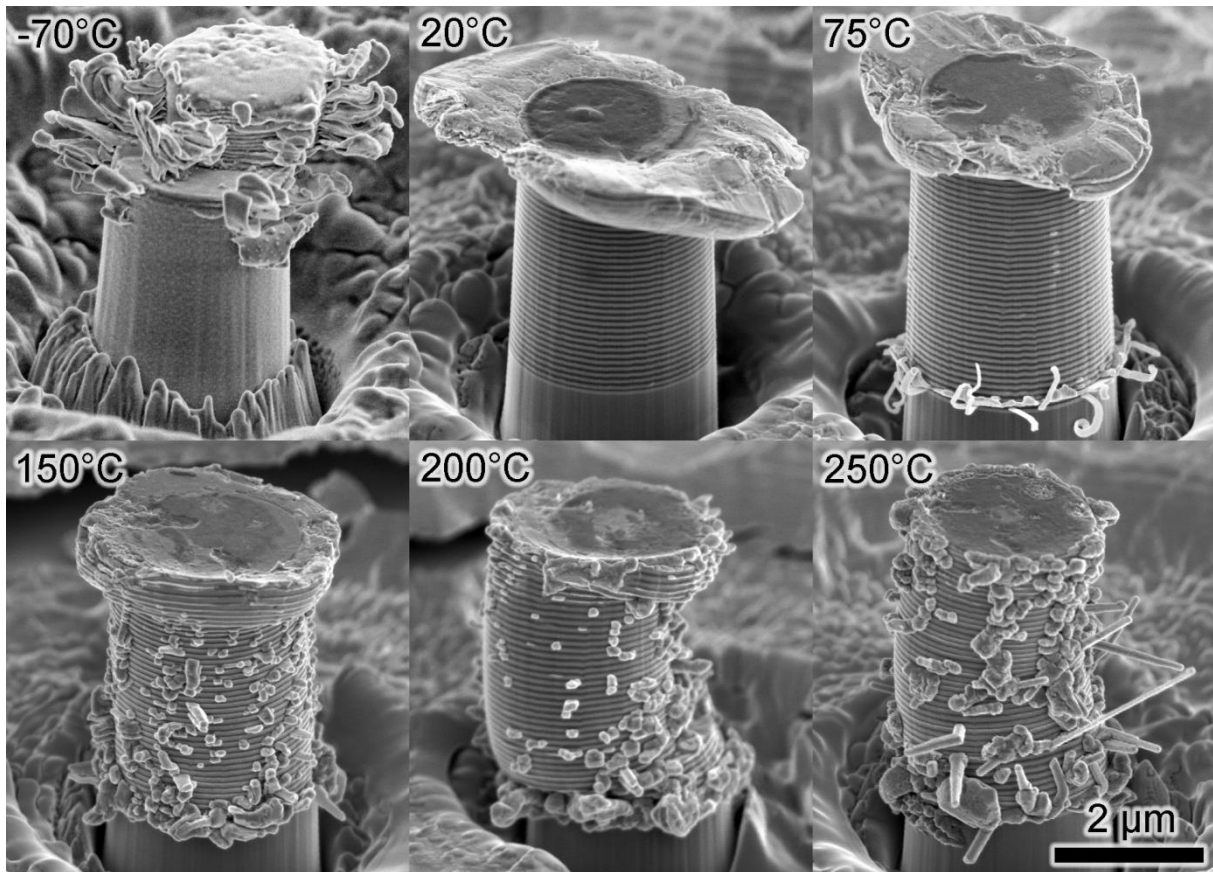


Figure 7: Micropillars with 50 nm layer thickness compressed at various temperatures

The 50 nm layer thickness micropillars demonstrate a much more marked change in deformation mechanism with temperature. At room temperature, the tapered top portion of the pillar accounts for nearly all of the plastic deformation, mushrooming out as the magnesium layers deform and the niobium layers fracture. At 72.5°C the mushrooming near the top of the pillar is far less pronounced and the magnesium layer nearest to the substrate has collapsed. Small, curved tendrils of magnesium have extruded from this lower magnesium layer. At temperatures of 150° and above the mushrooming effect near the top of the pillar has become much less pronounced while all of the magnesium layers contribute to the deformation of the pillar. This is evidenced by the growth of magnesium protuberances and whiskers from the outer surface of the pillar. EDS was used to confirm that these features consist exclusively of magnesium. At 250°C many of these whiskers clearly exhibit a hexagonal cross-section and sharp kinks indicative of an internal twin boundary or stacking fault. As is observed in the 5 nm thick layer samples at 250°C, the magnesium extrusions from the micropillar have begun to coalesce when they come into contact with magnesium extruded by adjacent layers. In all cases no growth of whiskers was observed during the roughly one-hour

temperature stabilization period, but rather occurred nearly instantaneously upon the application of mechanical load.

The differences on the deformation behaviors of the two layer thicknesses are also reminiscent of the differences between BCC and HCP Mg. Both the layer thicknesses show instability in their stress-strain response at room temperature after the peak stress levels are reached (Figure 15). However, the instability is less apparent with increasing temperatures for the 5 nm thick BCC Mg layers, where the flow stresses are maintained over an extended straining period. In contrast, the instability persists in the 50 nm thick HCP Mg layers even at the highest temperatures of 250°C. This is typical of HCP nanomaterials when compressed along their c-axis, as is done here [33]. In these cases, the deformation response is typically inhomogeneous and localized in multiple regions throughout the pillar.

3.4.3. Cryogenic Temperature Micropillar Compression

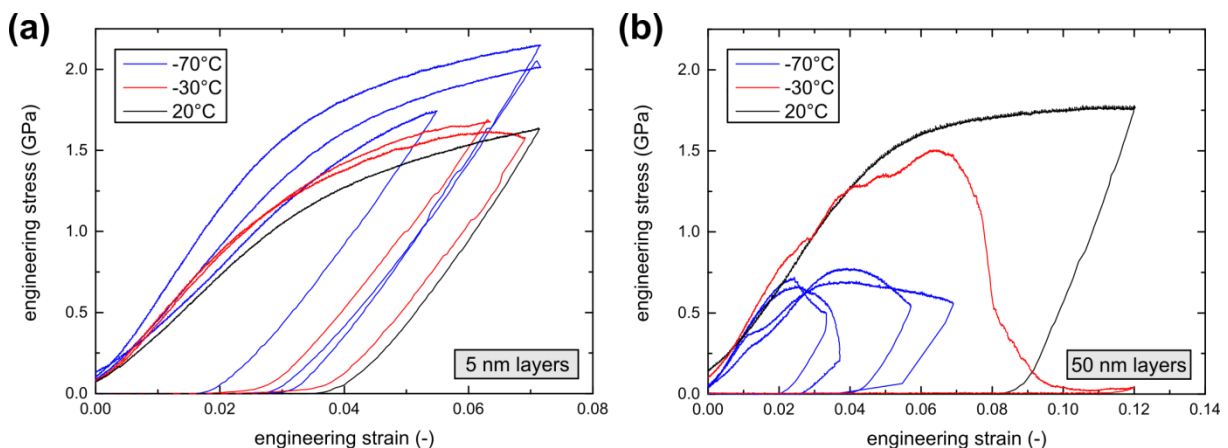


Figure 8: The Mg-Nb multilayer micropillars with 5 nm individual layer thickness (a) demonstrate increasing yield strength with decreasing temperature down to -70°C while the 50 nm Mg-Nb multilayer micropillars lose strength with decreasing temperature due to the onset of brittle fracture.

All samples had to be sputtered with a thin (~5 nm) layer of gold in order to avoid charging and allow for sufficient image quality to perform alignment of the flat punch. The low-temperature adhesive has exceptionally poor electrical conductivity and is quite prone to charging effects in the SEM. The 5 nm films exhibit increased yield strengths with decreasing temperature as expected, allowing for successful SRJ tests to be performed at -70°C as well. The cryogenic data is presented separately in Figure

18 rather than with the elevated temperature data in Figure 15 to maintain clarity and give a better impression of the statistical variability within the cryogenic data.

The 50 nm films exhibited an unexpected, drastic reduction in yield strength. Data obtained at -30°C generally exhibited stochastic variation, with marked differences in micro-pillar deformation behavior from one pillar to the next. The best curves are shown in Figure 18(b). At -70°C the data was much more repeatable and exhibited less statistical variation. Brittle materials tend to exhibit higher variability in the failure stress, indicating that the material has undergone a ductile-to-brittle transition at cryogenic temperatures. The yield stress of only around 0.7 GPa is much lower than expected. In order to ensure that there were no sample or pillar surface alignment issues, a pillar was compressed at room temperature without changing the experimental setup. The yield strength was 1.6 GPa, only slightly below that obtained during the previous experiments. Sample misalignment can therefore be ruled out as a cause for the low yield stress. Since the stresses from thermal expansion coefficient mismatch are quite mild (10s of MPa at most), there must be some other stress concentration within the pillar leading to fracture of the magnesium layers. Minor voids or even variability within the grain boundaries is sufficient to act as a failure initiation point. The post-compression SEM micrographs in Figure 17 indicate that the magnesium layers account for all of the plastic deformation. As was observed in the elevated temperature experiments, the magnesium has been extruded out of the pillars. Here, however, there is no evidence for diffusion (no rounding, coalescence of adjacent layers, no formation of hexagonal structures), but rather through slip parallel to the substrate.

3.4.4. Activation Energy Analysis

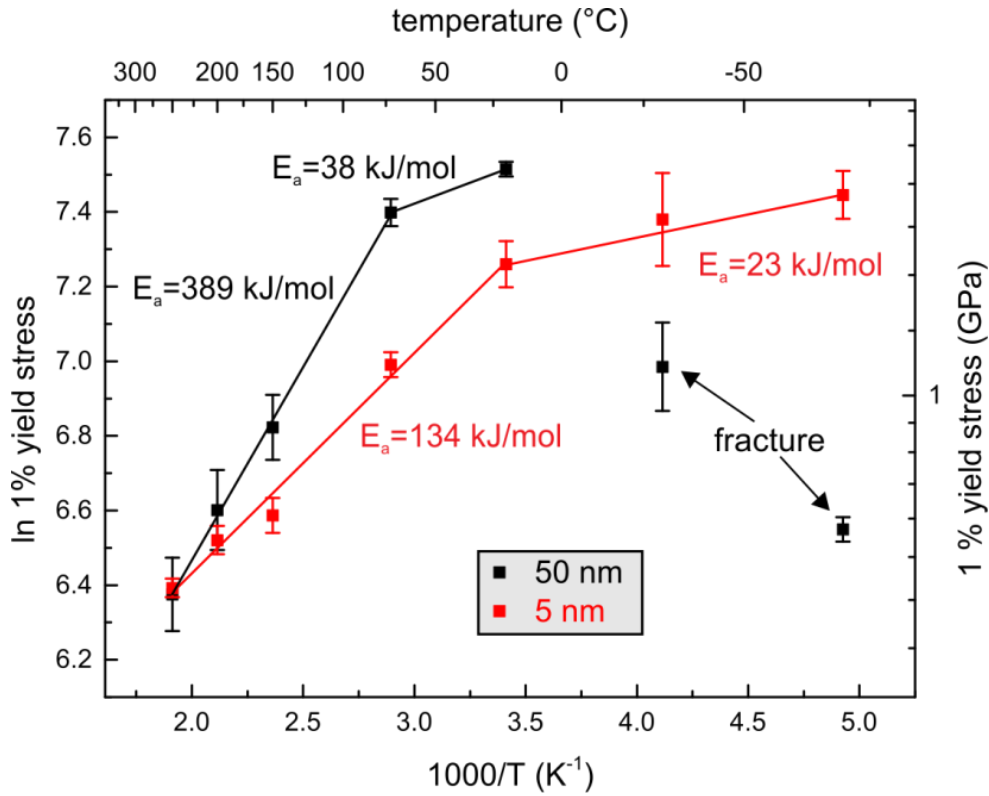


Figure 9: Arrhenius plot used for the calculation of activation energy for deformation mechanisms

The activation energy for the dominant deformation mechanisms was also calculated using the slope of the yield stress on an Arrhenius-style plot and the strain sensitivity exponent, as given by Equation 8.

$$Q = \frac{1}{m} R \left[\frac{\partial \ln \sigma}{\partial (1/T)} \right] \quad \text{Equation 4}$$

Activation energies for various deformation mechanisms in HCP magnesium include 135 kJ/mol for lattice diffusion, 92 kJ/mol for both boundary and core diffusion, and 230 kJ/mol for power-law creep [34]. No literature values for activation energies in BCC magnesium are available, therefore they are assumed to be similar to the values for HCP magnesium. Data regarding the diffusion coefficient of magnesium along a magnesium-niobium interface is also unavailable in the literature. It stands to reason that the value would lie somewhere between the grain boundary diffusion coefficient and the diffusion coefficient for a free surface. If this is the case, an activation volume of this magnitude is not unreasonable for a diffusion-dominated deformation mechanism. The flow stress was taken as being equivalent to the 1% yield offset stress determined from the elastic region of the loading curve.

4. Discussion

4.1. Microstructure

The Mg-Nb materials system was selected due to the mutual insolubility between the two materials, enabling multilayers with atomically sharp interfaces to be produced.

The TEM micrographs in

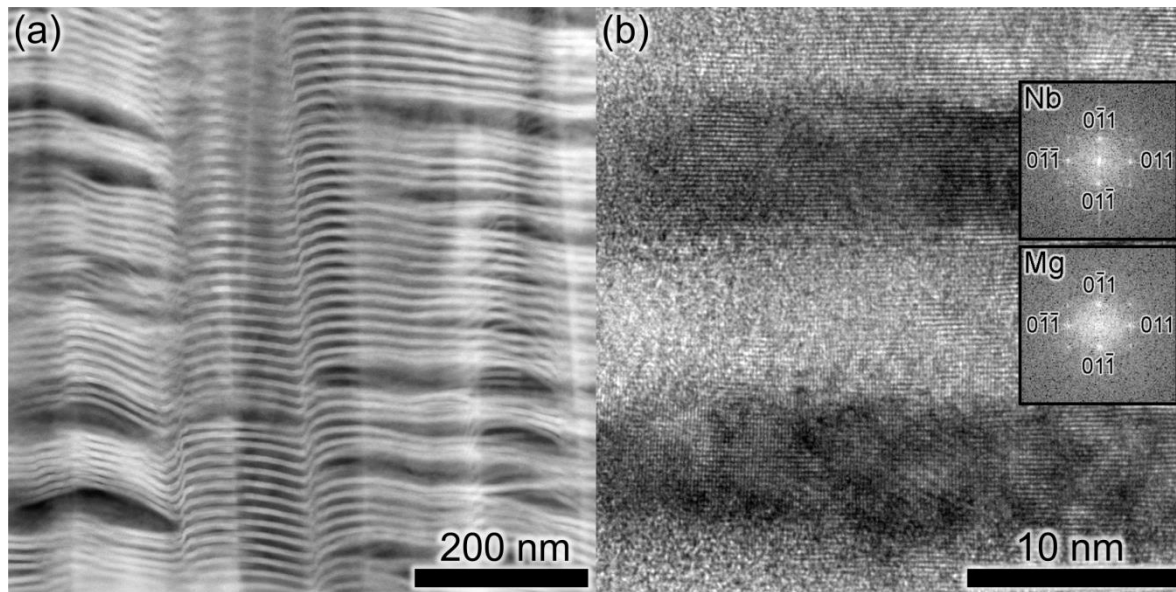


Figure 12 indicate that this was achieved and that the targeted BCC magnesium phase was also realized in the 5 nm layer thickness films. The preparation and imaging of TEM lamella is notably more labor-intensive than X-ray diffraction techniques, therefore the latter are preferable for determining the individual layer thicknesses and the phases present. The strong texture in sputtered films and the secondary peaks which appear for nanoscale multilayers complicate the interpretation of the XRD data, therefore TEM was used to confirm the findings.

Figure 10 shows the XRD results for both samples. When plotted linearly the Nb {110} and Nb {220} peaks are by far the most pronounced, indicating a strong {110} texture within the Nb layers. The Mg peaks are less intense due to the lower electron density in lighter elements. Phase identification can be convoluted by the presence of superlattice peaks which overlap with many of the classical XRD peaks. Significantly more superlattice peaks of higher intensity are observed here than were reported in reference [35]. This is due to the subtle differences in the precise individual layer thickness. The spacing of these peaks is very sensitive to the layer thickness and can also be

used to obtain an estimate of the layer thicknesses. More precise determination of layer thickness is obtained using XRR in Figure 11.

Density Functional Theory (DFT) simulations show that BCC magnesium is metastable under thin film conditions where magnesium grows epitaxially on BCC niobium [35]. Further DFT calculations predict a stability cutoff for BCC magnesium with a layer thickness of 4.2 nm [31], a value which is exceeded by the 7.9 nm Mg layer thickness here. The thickness of the BCC Mg layers could also likely be increased further through the use of higher volume fractions of Nb. The XRR data demonstrates that the density of the films is somewhat lower than bulk material. This is seen by the lower angles at which total external reflection ceases to operate and is more pronounced for the 5 nm film than for the 50 nm film. Cross-sections of the film do not reveal any obvious porosity or voids, so the films were considered to be sufficiently dense to perform mechanical tests. The possibility of film density impacting the mechanical properties of the films should still be taken into consideration.

4.2. Mechanical Behavior

For the elevated temperature tests there is a continuous decrease in yield strength for both layer thicknesses. This result is consistent with the theory that deformation consists of both thermal and athermal components and that the yield strength of a material decreases with increasing temperature. Previous nanoindentation experiments have studied the thermal stability of Mg-Nb multilayer films, by exposing them to temperatures of up to 200 °C and then cooling them down to room temperature before conducting indentation measurements [36], but the results shown in this work are the first to measure their properties under elevated temperature conditions.

Moreover, micropillar compression experiments provide a clearer result due to the more uniaxial stress state and the lack of large isostatic stresses from lateral confinement in nanoindentation experiments.

The overall behavior of the stress-strain curves is reminiscent of that of pure magnesium. HCP magnesium possesses a low ductility and initially high strain-hardening behavior due to the decomposition of dislocations into lower-energy, immobile arrangements [37]. At elevated temperatures magnesium exhibits limited strain-hardening capacity, resulting in rapidly reached peak stress followed by significant softening [38].

This behavior was also observed in this experiments and deformation is postulated to be dominated by the behavior of the magnesium layers. Niobium requires very high stresses to display any diffusion, regardless of the temperature, and does not contribute to the micropillar plasticity at elevated temperatures. This is also supported by the post-compression SEM micrographs which show that pillar failure is a result of plasticity within the magnesium layers, except at lower temperatures where co-deformation causes the niobium layers to crack. While the ductile-to-brittle transition temperature for pure niobium is well below the temperature range tested here [39], the introduction of even very small quantities of impurity atoms can result in the onset of brittle behavior at temperatures around -30°C [40].

In the samples with 5 nm layer thickness (those containing BCC magnesium) the pillars also exhibit a clear transition in deformation mechanism from diffusion- to dislocation-based deformation with decreasing temperature. In the 5 nm layer thickness films this transitions occurs around room temperature, rather than 75°C as observed for the 50 nm layer thickness films. The general mode of failure begins with the formation of a shear band that forms from the upper edge of the micropillar. At lower temperatures this shear band behaves like a wedge and ultimately displaces the lower part of the pillar from its substrate pedestal. At higher temperatures the micropillar is capable of accommodating larger deformations without separating from the substrate pedestal. Agglomerated magnesium protuberances form on the pillar surface at higher temperatures. At the highest temperatures the silicon pedestal appears to be compromised where the stress is the highest. A long filament is often observed growing out from this point. It seems like that this filament is also a magnesium whisker, albeit much thinner than those observed in the 50 nm layer thickness samples.

The 50 nm layers exhibit a stress concentration at the top of the pillar due to taper which causes the upper part of the pillar to deform first at lower temperatures. As the temperature increases the bottom layers instead fail first, with more of a curling, extruded appearance rather than the whiskers seen from the upper layers. The stress concentration at the base of the pillar is a result of the elastic modulus mismatch between the substrate and film, otherwise known as image stress. The reduced interface roughness could also play a role as the smoother silicon-magnesium interface provides

less resistance to lateral forces, whereas in the upper layers of the film a compound waviness prevents any lateral sliding.

Contrary to prior reports of room temperature micropillar compression of similar films [36], the “smaller is stronger” mantra is not followed. There is good agreement between the values for 50 nm layer thicknesses, so presumably the 5 nm layer thickness films presented here are not entirely dense. The TEM cross-sections do not exhibit porosity or voids within the grains while the SEM micrographs indicate that the reduced density can be accounted for by the grain boundaries. It is also possible that the enhanced strain rate sensitivity of the thinner layers coupled with the relatively low strain rates results in somewhat lower yield stress. Direct comparison between the two-layer thicknesses is further complicated by the different magnesium phases. As such the quantitative strength values for the 5 nm films presented here should be treated with some skepticism, but the activation energy and activation volume are expected to be representative of a fully dense film. Micropillar compression is ideal for testing thin films as these types of multilayered structures are not easily realizable in bulk samples. First strain rate jump, and then variable temperature micropillar compressions tests are performed, permitting the activation energy to be calculated by using the strain rate sensitivity information gained from the strain rate jump tests. This approach of coupling SRJ tests with variable temperature testing to gain insight into the operative deformation mechanisms has been previously used in nanocrystalline nickel [19].

The Arrhenius plot of the 1% yield stress values is used together with the strain-rate sensitivity exponent calculated from the strain rate jump tests in order to calculate the activation energy of deformation, as shown in Figure 19. The 5 nm film data points are collinear in the Arrhenius plot, indicating that there is no change in the operational deformation mechanism. The activation energy of 134 kJ/mol is well above those reported for dislocation-based deformation mechanisms and agrees well with the values reported for diffusion. Diffusion can occur readily as each interface between magnesium and niobium within the multilayer film serves as a potential diffusion pathway. Experimental tensile test results for bulk magnesium and magnesium alloys performed between 423 and 773 K [38] report the activation energy for pure magnesium as ranging from 20 to 270 kJ/mol, increasing with increasing temperature. The magnesium alloy, however, remains confined between 92 kJ/mol for pipe diffusion [34] and 135

kJ/mol for lattice self-diffusion [41]. Similar activation energies between 100 and 110 kJ/mol were measured in AZ31 magnesium alloy and were attributed to either dislocation creep climb associated with pipe diffusion or simple lattice diffusion [42]. The 50 nm layer thickness films, however, exhibit a change in the activation energy 72.5°C. At lower temperatures the activation energy is around 38 kJ/mol. This value lies between those reported for dislocation movement and diffusion, indicating that both mechanisms contributing to the overall plasticity. At higher temperatures the yield strength drops drastically with increasing temperature and the activation energy reaches 389 kJ/mol, a value even beyond that reported for lattice diffusion. Such high activation energies are indicative of dynamic recrystallization [43].

Similar signs of plasticity facilitated by diffusion in multilayer micropillars have been observed previously, albeit at a lower homologous temperature. The surface extrusions were described as “tongues” of aluminum extruded from 60 nm layer thickness Al-SiC multilayers compressed at 100°C (homologous temperature of 0.4 for aluminum). [44] Interface sliding was cited as the main deformation mechanism. Interface sliding was modeled using FEM while treating the Al-SiC interface as a cohesive crack. A reduced friction coefficient was introduced after the cohesive crack is broken. The interface sliding model did not account for the asymmetry of the extrusions and the possibility of interfacial diffusion is briefly mentioned in the conclusions. Nanoindentation performed on these same layers [45] did not show the same degree of strain hardening as the lateral flow of aluminum is prevented through the surrounding material, indicating that the free surface of a micropillar is necessary for such strain hardening to occur. The bottom layer of these micropillars was also observed to deform prior to the rest of the layers and was commented upon, but no explanation was proposed. An elastic mismatch between the film and substrate is the likely culprit here as well. A recent nanoindentation study of Al-SiC multilayers demonstrate that multilayers with thinner layers exhibit inferior yield stress compared to thicker multilayers at elevated temperatures [46]. Grain boundary and interface diffusion are concluded to limit the strength of aluminum multilayers at elevated temperatures (up to 100°C).

The cryogenic tests for the 5 nm layer thickness films follow the same trend as the elevated temperature tests, with increasing strength at lower temperatures. These observations are in agreement with previous experiments in magnesium alloys. At room

temperature, AZ31B magnesium alloy exhibits some ductility before fracture, whereas when cooled to liquid nitrogen (77K) and liquid helium (4.2K), fracture is entirely brittle. The strength is observed to increase continuously with decreasing temperature [47]. For bulk specimens, a brittle-to-ductile transition temperature has been reported to be as high as 200°C when ductility is provided through dynamic recrystallization [48]. No direct comparison with bulk cubic magnesium is possible as it is only stable at extremely high pressures. The 50 nm films, however, exhibit somewhat surprising yielding behavior. The yield strength is reduced drastically below that observed at room temperature. The failure mechanism here is clearly a different one than observed at room temperature and elevated temperatures, with significant glide occurring within the magnesium layers along their basal plane. The magnesium layers have fractured and been ejected out of the micropillar at higher strains. While superficially similar to the magnesium protuberances observed at elevated temperatures, there are no signs of diffusion having contributed to deformation. There is no edge rounding, formation of whiskers, or coalition of adjacent layers. Instead brittle fracture has occurred at internal stress concentrations and the magnesium layers are ejected from the pillars through basal glide. At the lowest temperatures measured here fracture of the niobium layers is possible as well due to the ductile-to-brittle transition in Niobium when impurities are present.

The conventional hardening models used for describing the strength of multilayers all rely on dislocation-based mechanisms. Around room temperature the 50 nm multilayers still benefit from these strengthening mechanisms, as described by the confined layer slip model. The original model proposed by Misra *et al.* [8] was then modified to include an additional two strength contributors: elastic interface stress (f) and interactions between confined layer slip dislocations and those already present near the interfaces (C/λ).

At 5 nm layer thickness, however, there is no longer sufficient space for a dislocation to bow between interfaces. Instead the properties of the interface dictate yield strength. Activation volume in BCC materials tends to be small as yield stress is strongly dependent upon temperature [49], and this effect is even more pronounced in a material with a low melting temperature like magnesium. The introduction of a large number of internal interfaces provides numerous pathways along which magnesium can readily

diffuse. The use of a model based solely on dislocation movement is not valid for describing the type of behavior observed in Mg-Nb multilayers across the temperature range investigated here. Further studies are needed in both this and other materials systems in order to develop a model which can be used to predict material strength where diffusion and brittle fracture can occur.

5. Conclusion

Pseudomorphic BCC magnesium has been stabilized in Mg-Nb multilayers at thicknesses of more than 7 nm. Micropillar compression tests at both cryogenic and elevated temperatures were used to calculate the activation energy and activation volume governing the mechanical behavior of the films. Mg-Nb multilayer films with individual layer thicknesses of 5 and 50 nm demonstrate two major deformation regimes: an elevated temperature regime where deformation is controlled by diffusional flow of magnesium and a lower temperature regime where dislocation movement and co-deformation of the layers dictates the material behavior. At cryogenic temperatures the 50 nm layer thickness films fail via brittle fracture of the niobium layers and within the magnesium layers through glide along their basal plane. Around room temperature a combination of dislocation- and diffusion-based mechanisms are active, where enhanced plasticity prevents the type of brittle fracture and glide observed at cryogenic temperatures. At elevated temperatures deformation is dominated by diffusion, where the growth of magnesium whiskers outside the micropillar occurs during deformation. The lower-than-expected strength of the 5 nm layer thickness films is attributed to non-fully dense magnesium layers and the relatively low strain rates applied, though the deformation mechanisms are postulated to remain unaffected relative to fully dense films.

6. Acknowledgements

The research leading to these results has received funding from STEEP, a Marie Curie Action Initial Training Network (ITN) of the European Union's Seventh Framework Program FP7 under REA grant agreement number 316560. The open and friendly atmosphere at both LANL and Empa has enabled this international collaboration. This work was performed in part at the Center for Integrated Nanotechnologies, an Office of Science User Facility operated for the U.S. Department of Energy (DOE) Office of

Science. Los Alamos National Laboratory, an affirmative action equal opportunity employer, is operated by Los Alamos National Security, LLC, for the National Nuclear Security Administration of the U.S. Department of Energy under contract DE-AC52-06NA25396. Alemnis is also gratefully acknowledged for the development of the in-instrumentation and methodology used to perform the cryogenic tests.

7. References

- [1] N. Matuschek, F.X. Kartner, U. Keller, Exact coupled-mode theories for multilayer interference coatings with arbitrary strong index modulations, *IEEE J. Quantum Electron.* 33 (1997) 295–302. doi:10.1109/3.555995.
- [2] A. Bergmann, D. Orthaber, G. Scherf, O. Glatter, Improvement of SAXS measurements on Kratky slit systems by Göbel mirrors and imaging-plate detectors, *J. Appl. Crystallogr.* 33 (2000) 869–875. doi:10.1107/S0021889800000881.
- [3] Y. Fink, J.N. Winn, S. Fan, C. Chen, J. Michel, J.D. Joannopoulos, E.L. Thomas, A dielectric omnidirectional reflector, *Science* (80-.). 282 (1998) 1679–1682. doi:10.1126/science.282.5394.1679.
- [4] H. Rong, R. Jones, A. Liu, O. Cohen, D. Hak, A. Fang, M. Paniccia, A continuous-wave Raman silicon laser, *Nature.* 433 (2005) 725–728. doi:10.1038/nature03346.
- [5] A.I. Zhmakin, Enhancement of light extraction from light emitting diodes, *Phys. Rep.* 498 (2011) 189–241. doi:10.1016/j.physrep.2010.11.001.
- [6] J. Wang, a. Misra, An overview of interface-dominated deformation mechanisms in metallic multilayers, *Curr. Opin. Solid State Mater. Sci.* 15 (2011) 20–28. doi:10.1016/j.cossms.2010.09.002.
- [7] W.A. Jesser, J. Kui, Misfit dislocation generation mechanisms in heterostructures, *Mater. Sci. Eng. A.* 164 (1993) 101–110. doi:10.1016/0921-5093(93)90647-W.
- [8] A. Misra, J.P. Hirth, R.G. Hoagland, Length-scale-dependent deformation mechanisms in incoherent metallic multilayered composites, *Acta Mater.* 53 (2005) 4817–4824. doi:10.1016/j.actamat.2005.06.025.
- [9] J. Wang, C. Yang, P.D. Hodgson, Strain gradients in Cu–Fe thin films and multilayers during micropillar compression, *Mater. Sci. Eng. A.* 651 (2016) 146–154. doi:10.1016/j.msea.2015.10.105.
- [10] B. Ham, X. Zhang, High strength Mg/Nb nanolayer composites, *Mater. Sci. Eng. A.* 528 (2011) 2028–2033. doi:10.1016/j.msea.2010.10.101.
- [11] G.B. Thompson, R. Banerjee, H.L. Fraser, Predicting pseudomorphic phases in multilayers: Hexagonal-closed-packed Nb in Nb/Zr, *Appl. Phys. Lett.* 84 (2004) 1082–1084. doi:10.1063/1.1647687.
- [12] W.P. Lowe, T.H. Geballe, NbZr multilayers. I. Structure and superconductivity, *Phys. Rev. B.* 29 (1984) 4961–4968. doi:10.1103/PhysRevB.29.4961.
- [13] D. Van Heerden, D. Josell, D. Shechtman, The formation of f.c.c. Titanium in titanium-aluminum multilayers, *Acta Mater.* 44 (1996) 297–306. doi:10.1016/1359-6454(95)00159-5.
- [14] R. Ahuja, H.L. Fraser, Microstructural transitions in Titanium-Aluminum thin film multilayers, *J. Electron. Mater.* 23 (1994) 1027–1034. doi:10.1007/BF02650371.
- [15] S.A. Dregia, R. Banerjee, H.L. Fraser, Polymorphic phase stability in thin

- multilayers, *Scr. Mater.* 39 (1998) 217–223. doi:10.1016/S1359-6462(98)00144-4.
- [16] J.C. Li, W. Liu, Q. Jiang, Bi-phase transition diagrams of metallic thin multilayers, *Acta Mater.* 53 (2005) 1067–1071. doi:10.1016/j.actamat.2004.11.004.
- [17] J.M. Wheeler, P. Brodard, J. Michler, Elevated temperature, *in situ* indentation with calibrated contact temperatures, *Philos. Mag.* 92 (2012) 3128–3141. doi:10.1080/14786435.2012.674647.
- [18] J.S. Carpenter, A. Misra, M.D. Uchic, P.M. Anderson, Strain rate sensitivity and activation volume of Cu/Ni metallic multilayer thin films measured via micropillar compression, *Appl. Phys. Lett.* 101 (2012). doi:10.1063/1.4739521.
- [19] G. Mohanty, J.M. Wheeler, R. Raghavan, J. Wehrs, M. Hasegawa, S. Mischler, L. Philippe, J. Michler, Elevated temperature, strain rate jump microcompression of nanocrystalline nickel, *Philos. Mag.* 95 (2014) 1878–1895. doi:10.1080/14786435.2014.951709.
- [20] J. Ast, J.J. Schwiedrzik, J. Wehrs, D. Frey, M.N. Polyakov, J. Michler, X. Maeder, The brittle-ductile transition of tungsten single crystals at the micro-scale, *Mater. Des.* 152 (2018) 168–180. doi:10.1016/J.MATDES.2018.04.009.
- [21] I.K. Schuller, New Class of Layered Materials, *Phys. Rev. Lett.* 44 (1980) 1597–1600. doi:10.1103/PhysRevLett.44.1597.
- [22] M. Callisti, T. Polcar, Combined size and texture-dependent deformation and strengthening mechanisms in Zr/Nb nano-multilayers, *Acta Mater.* 124 (2017) 247–260. doi:10.1016/j.actamat.2016.11.007.
- [23] E.E. Fullerton, I.K. Schuller, H. Vanderstraeten, Y. Bruynseraede, Structural refinement of superlattices from x-ray diffraction, *Phys. Rev. B.* 45 (1992) 9292–9310. doi:10.1103/PhysRevB.45.9292.
- [24] A.H. Eltoukhy, J.E. Greene, Compositionally modulated sputtered InSb/GaSb superlattices: Crystal growth and interlayer diffusion, *J. Appl. Phys.* 50 (1979) 505–517. doi:10.1063/1.325643.
- [25] Q. Yang, C. He, L.R. Zhao, J.P. Immarigeon, Preferred orientation and hardness enhancement of TiN/CrN superlattice coatings deposited by reactive magnetron sputtering, *Scr. Mater.* 46 (2002) 293–297. doi:10.1016/S1359-6462(01)01241-6.
- [26] S. Pathak, N. Li, X. Maeder, R.G. Hoagland, J.K. Baldwin, J. Michler, A. Misra, J. Wang, N.A. Mara, On the origins of hardness of Cu–TiN nanolayered composites, *Scr. Mater.* 109 (2015) 48–51. doi:10.1016/J.SCRIPTAMAT.2015.07.015.
- [27] J. Wehrs, M.J. Deckarm, J.M. Wheeler, X. Maeder, R. Birringer, S. Mischler, J. Michler, Elevated temperature, micro-compression transient plasticity tests on nanocrystalline Palladium-Gold: Probing activation parameters at the lower limit of crystallinity, *Acta Mater.* 129 (2017) 124–137. doi:10.1016/j.actamat.2017.02.045.
- [28] E. Hart, Theory of the tensile test, *Acta Metall.* 15 (1967) 351–355. doi:10.1016/0001-6160(67)90211-8.
- [29] R.W. Cahn, D. Caillard, J.-L. Martin, Index, in: D. Caillard, J.L. Martin (Eds.), *Therm. Act. Mech. Cryst. Plast.*, Pergamon, 2003: pp. 57–82. doi:https://doi.org/10.1016/S1470-1804(03)80034-2.
- [30] Q. Wei, S. Cheng, K.T. Ramesh, E. Ma, Effect of nanocrystalline and ultrafine grain sizes on the strain rate sensitivity and activation volume: Fcc versus bcc metals, *Mater. Sci. Eng. A.* 381 (2004) 71–79. doi:10.1016/j.msea.2004.03.064.
- [31] A. Kumar, I.J. Beyerlein, J. Wang, First-principles study of the structure of

- Mg/Nb multilayers, *Appl. Phys. Lett.* 105 (2014). doi:10.1063/1.4893700.
- [32] M. Ardeljan, M. Knezevic, M. Jain, S. Pathak, A. Kumar, N. Li, N.A. Mara, J.K. Baldwin, I.J. Beyerlein, Room temperature deformation mechanisms of Mg/Nb nanolayered composites, *J. Mater. Res.* 33 (2018) 1311–1332. doi:10.1557/jmr.2018.107.
- [33] M.W. Kapp, A. Hohenwarter, S. Wurster, B. Yang, R. Pippin, Anisotropic deformation characteristics of an ultrafine- and nanolamellar pearlitic steel, *Acta Mater.* 106 (2016) 239–248. doi:10.1016/J.ACTAMAT.2015.12.037.
- [34] H.J. Frost, M.F. Ashby, *Deformation-mechanism maps: the plasticity and creep of metals and ceramics*, Pergamon Press, 1982. <https://books.google.ch/books?id=s9BRAAAAMAAJ>.
- [35] A.R. Junkaew A, Ham B, Zhang X, Talapatra A, A. Junkaew, B. Ham, X. Zhang, Stabilization of bcc Mg in Thin Films at Ambient Pressure: Experimental Evidence and ab initio Calculations, *Mater. Res. Lett.* 1 (2013) 161–167. doi:10.1080/21663831.2013.804218.
- [36] S. Pathak, N. Velisavljevic, J.K. Baldwin, M. Jain, S. Zheng, N.A. Mara, I.J. Beyerlein, Strong, Ductile, and Thermally Stable bcc-Mg Nanolaminates, *Sci. Rep.* 7 (2017) 8264. doi:10.1038/s41598-017-08302-5.
- [37] Z. Wu, W.A. Curtin, The origins of high hardening and low ductility in magnesium, *Nature.* 526 (2015) 62–67. doi:10.1038/nature15364.
- [38] A. Galiyev, O. Sitdikov, R. Kaibyshev, Deformation Behavior and Controlling Mechanisms for Plastic Flow of Magnesium and Magnesium Alloy, *Mater. Trans.* 44 (2003) 426–435. doi:10.2320/matertrans.44.426.
- [39] M.A. Adams, A.C. Roberts, R.E. Smallman, Yield and fracture in polycrystalline niobium, *Acta Metall.* 8 (1960) 328–337. doi:10.1016/0001-6160(60)90118-8.
- [40] M.L. Grossbeck, H.K. Birnbaum, Low temperature hydrogen embrittlement of niobium II—Microscopic observations, *Acta Metall.* 25 (1977) 135–147. doi:10.1016/0001-6160(77)90117-1.
- [41] P. Shewmon, F. Rhines, Rate of self-diffusion in polycrystalline magnesium, *J. Met.* (1954). <http://www.osti.gov/scitech/biblio/4408928>.
- [42] H.-K. Kim, W.-J. Kim, Creep behavior of AZ31 magnesium alloy in low temperature range between 423 K and 473 K, *J. Mater. Sci.* 42 (2007) 6171–6176. doi:10.1007/s10853-006-1162-9.
- [43] C. Roucoules, P.D. Hodgson, S. Yue, J.J. Jonas, Softening and microstructural change following the dynamic recrystallization of austenite, *Metall. Mater. Trans. A.* 25 (1994) 389–400. doi:10.1007/BF02647984.
- [44] S. Lotfian, M. Rodríguez, K.E. Yazzie, N. Chawla, J. Llorca, J.M. Molina-Aldareguía, High temperature micropillar compression of Al/SiC nanolaminates, *Acta Mater.* 61 (2013) 4439–4451. doi:10.1016/j.actamat.2013.04.013.
- [45] S. Lotfian, J.M. Molina-Aldareguia, K.E. Yazzie, J. Llorca, N. Chawla, High-temperature nanoindentation behavior of Al/SiC multilayers, *Philos. Mag. Lett.* 92 (2012) 362–367. doi:10.1080/09500839.2012.674220.
- [46] L.W. Yang, C. Mayer, N. Chawla, J. Llorca, J.M. Molina-Aldareguía, Deformation mechanisms of ultra-thin Al layers in Al/SiC nanolaminates as a function of thickness and temperature, *Philos. Mag.* 96 (2016) 3336–3355. doi:10.1080/14786435.2016.1219075.
- [47] X.D. Jiao, Mechanical Properties of Low Density Alloys at Cryogenic Temperatures, *AIP Conf. Proc.* 824 (2006) 69–76. doi:10.1063/1.2192335.
- [48] T. Al-Samman, G. Gottstein, Dynamic recrystallization during high temperature deformation of magnesium, *Mater. Sci. Eng. A.* 490 (2008) 411–420. doi:10.1016/J.MSEA.2008.02.004.

- [49] G. Taylor, Thermally-activated deformation of BCC metals and alloys, *Prog. Mater. Sci.* 36 (1992) 29–61. doi:10.1016/0079-6425(92)90004-Q.

List of Figures

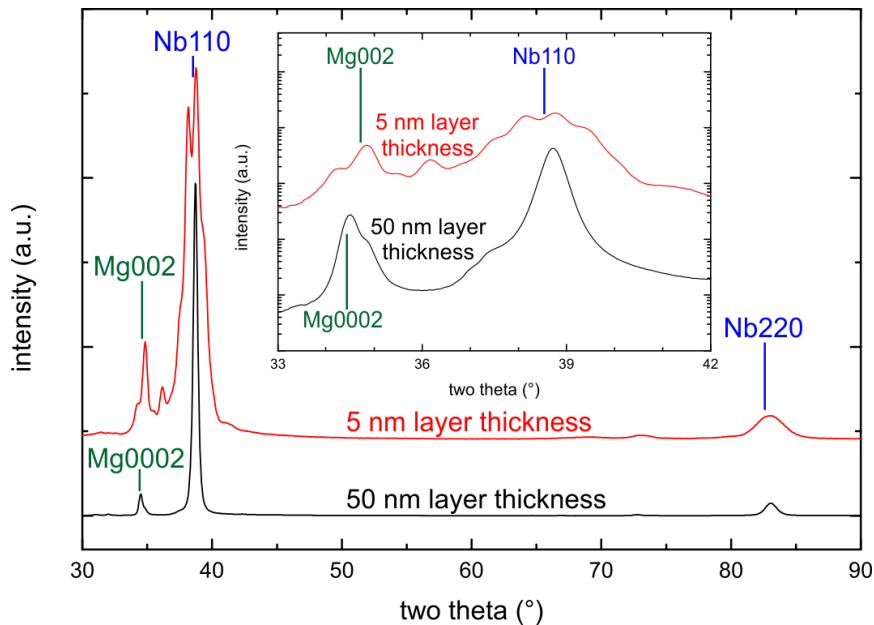


Figure 10: Bragg-Brentano XRD patterns for both 5 and 50 nm layer thicknesses in Mg-Nb multilayers. Superlattice peaks are apparent between 33° and 42° for the films with a layer thickness of 5 nm, indicating an epitaxial relationship between Mg and Nb for thin layer thicknesses.

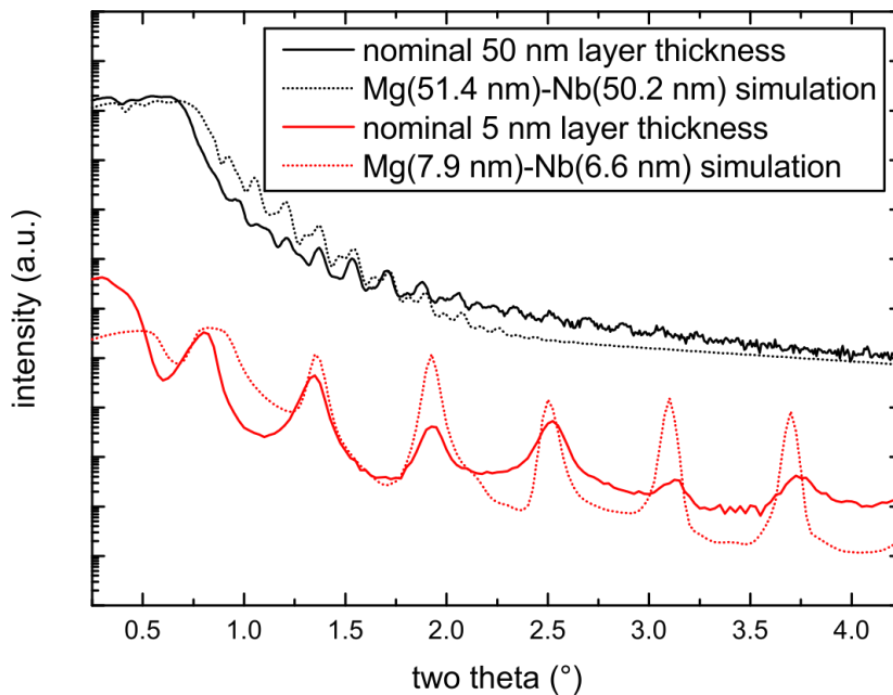


Figure 11: X-Ray Reflectometry (XRR) curves, both as measured and as simulated for Mg-Nb multilayers with nominal 5 and 50 nm layer thicknesses.

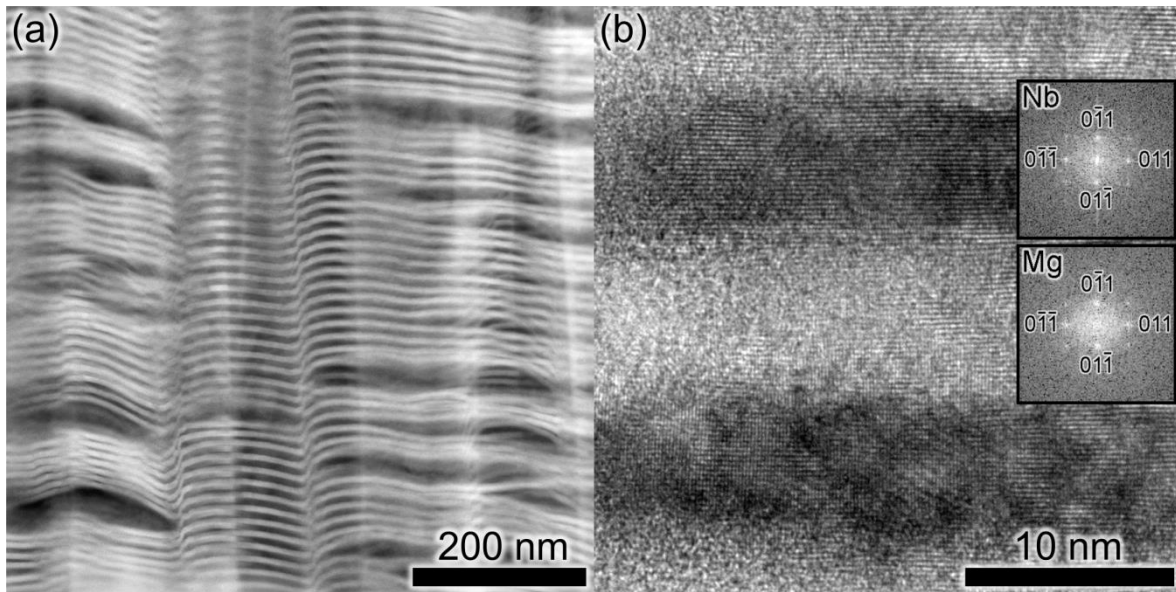


Figure 12: Cropped and rotated (a) HAADF-STEM and (b) HRTEM image with FFT inset of Mg-Nb multilayer with 5 nm layer thickness

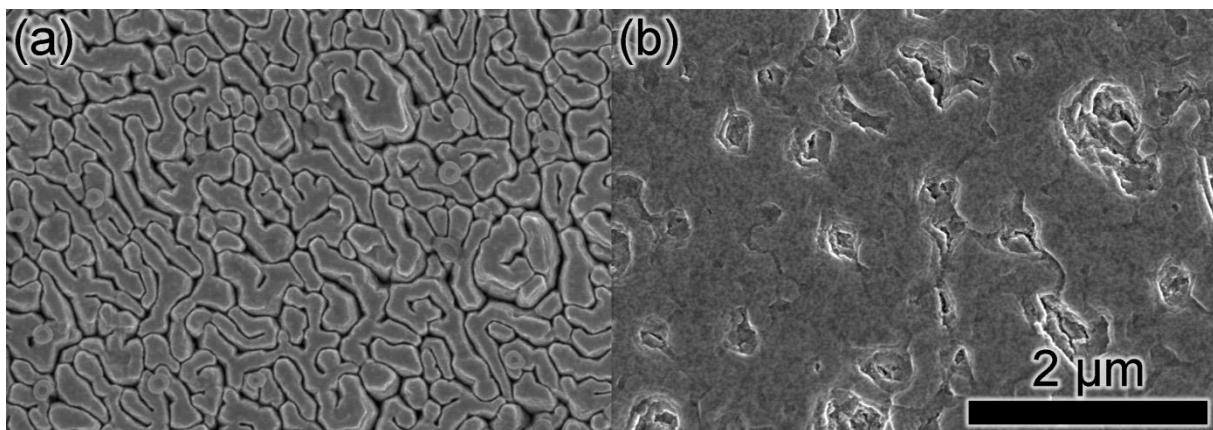


Figure 13: Characteristic surface topology of (a) 5 nm and (b) 50 nm layer thickness Mg-Nb films

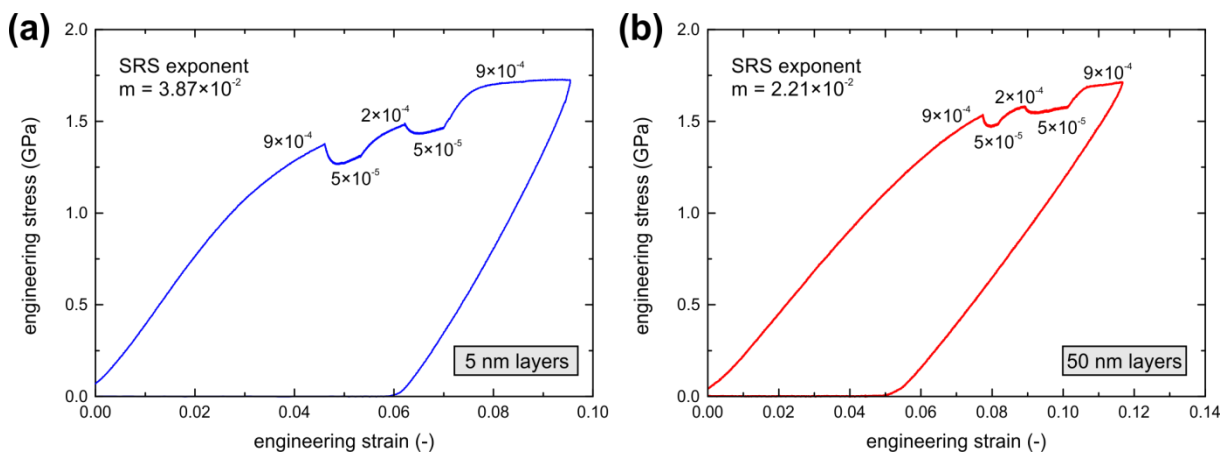


Figure 14: Strain Rate Jump (SRJ) results for Mg-Nb multilayers with (a) 5 nm layer thickness and (b) 50 nm layer thickness

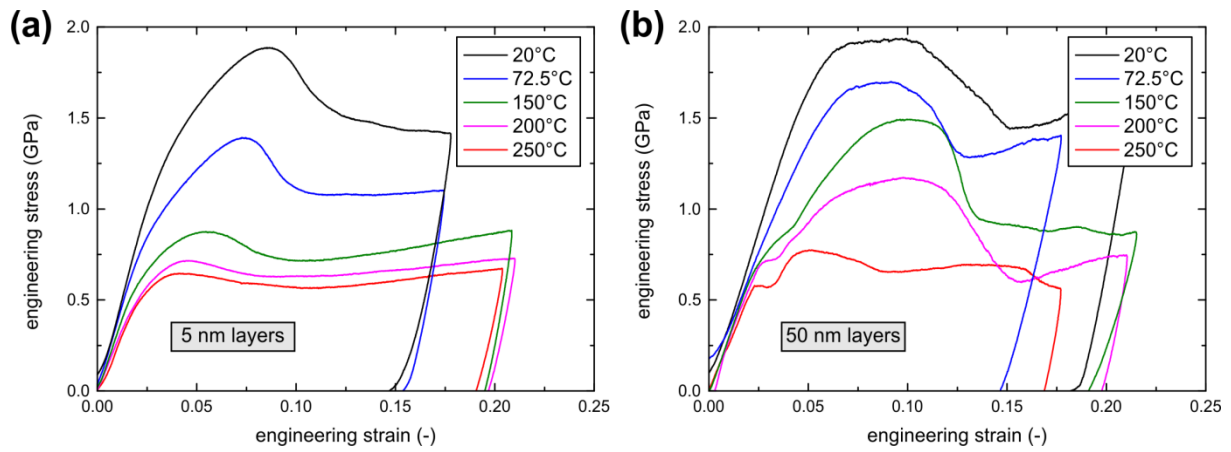


Figure 15: Engineering stress-strain curves for Mg-Nb multilayers with (a) 5 nm layer thickness and (b) 50 nm layer thickness at elevated temperatures

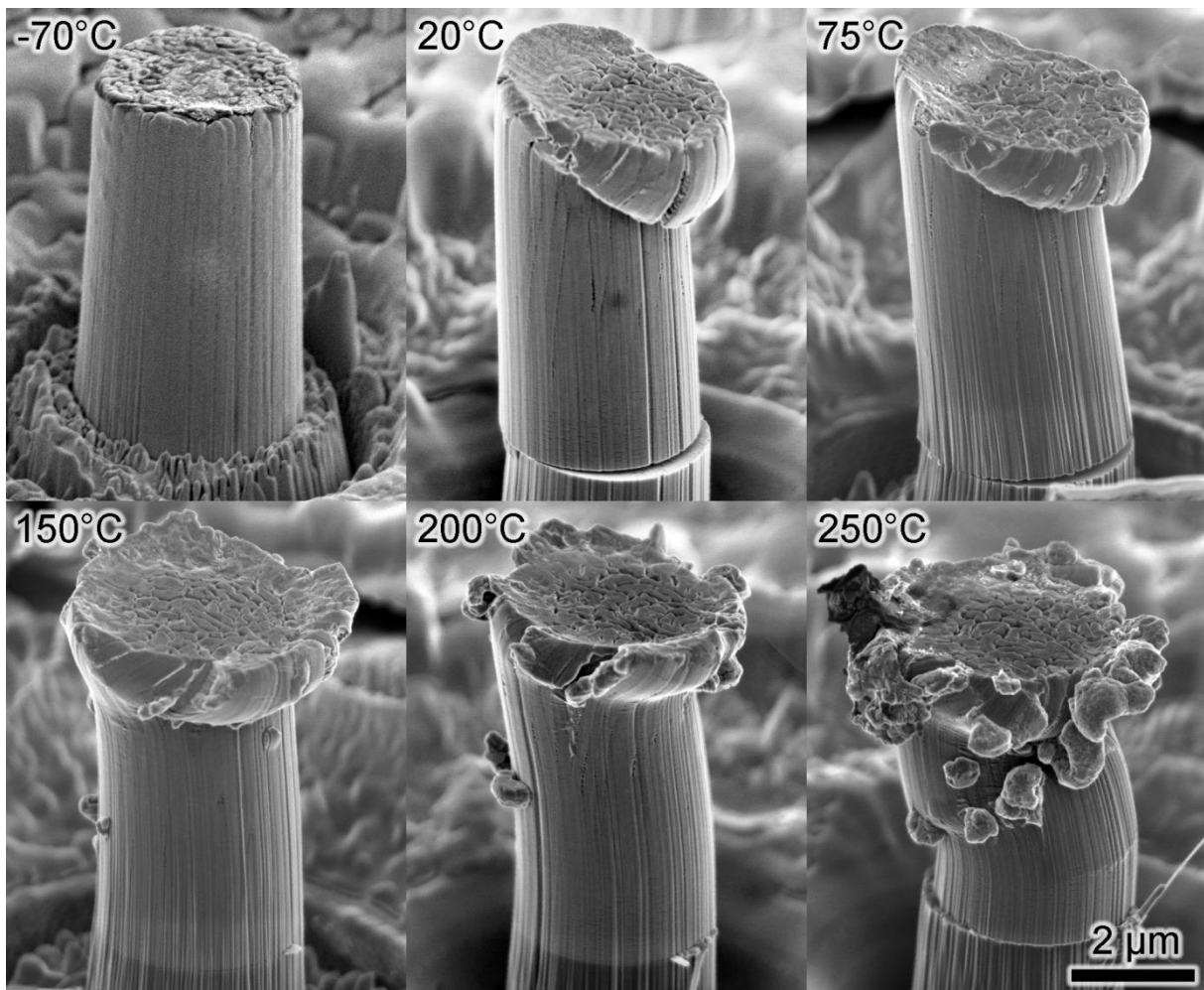


Figure 16: Micropillars with 5 nm layer thickness compressed at various temperatures

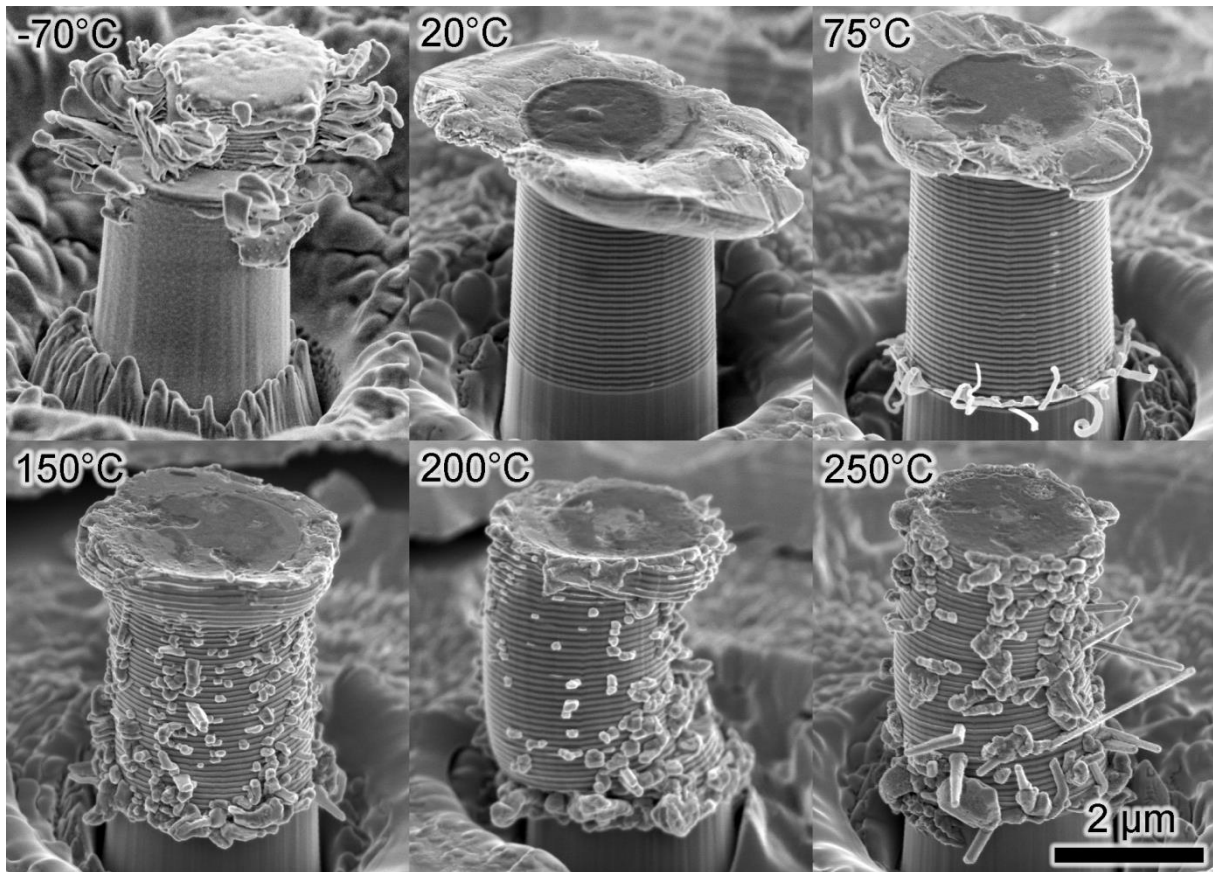


Figure 17: Micropillars with 50 nm layer thickness compressed at various temperatures

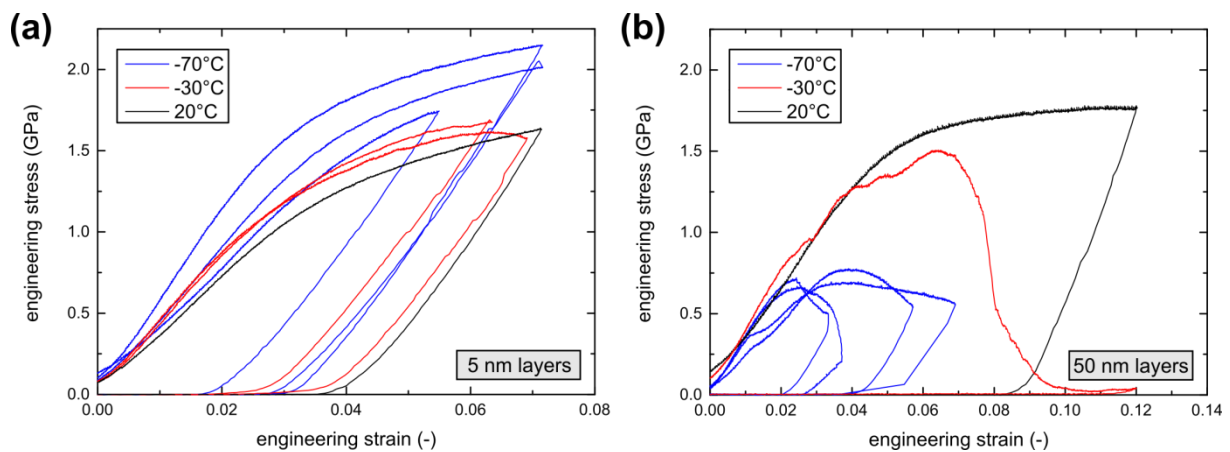


Figure 18: The Mg-Nb multilayer micropillars with 5 nm individual layer thickness (a) demonstrate increasing yield strength with decreasing temperature down to -70°C while the 50 nm Mg-Nb multilayer micropillars lose strength with decreasing temperature due to the onset of brittle fracture.

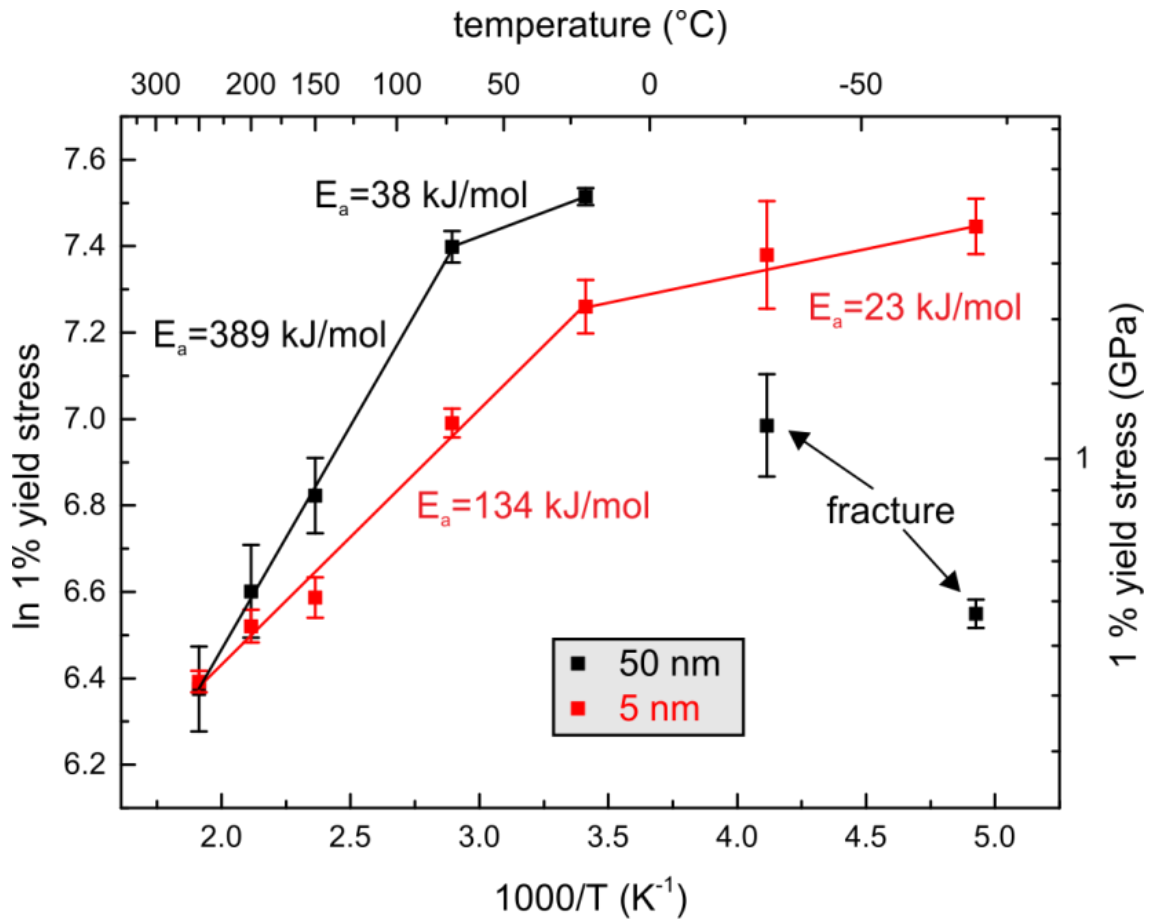


Figure 19: Arrhenius plot used for the calculation of activation energy for deformation mechanisms

List of Tables

Table 3: Sputter deposition conditions

	film 1	film 2
targeted individual layer thickness	5 nm	50 nm
base pressure	5·10 ⁻⁷ Torr	5·10 ⁻⁷ Torr
deposition pressure	6 mTorr	6 mTorr
Nb deposition power	300 Watts	300 Watts
Mg deposition power	300 Watts	300 Watts
Nb cycle duration	9.30 s	93.0 s
Mg cycle duration	2.03 s	20.3 s
# of bilayer cycles	500	50
nominal film thickness	5 μm	5 μm

List of Equations

$$\sin \theta_{\pm} = \sin \theta_B \pm \frac{n\lambda}{2\Lambda} \quad \text{Equation 5}$$

$$m = \left. \frac{\partial \ln \sigma}{\partial \ln \dot{\epsilon}} \right|_T \quad \text{Equation 6}$$

$$V_{\text{activation, apparent}} = \frac{\sqrt{3}kT}{m\sigma_f} \quad \text{Equation 7}$$

$$Q = \frac{1}{m} R \left[\frac{\partial \ln \sigma}{\partial (1/T)} \right] \quad \text{Equation 8}$$